Received: 11 December 2023 | Revised: 24 February 2024 | Accepted: 2 March 2024

DOI: 10.1002/nme.7478

RESEARCH ARTICLE

WILEY

On the role of tissue mechanics in fluid–structure interaction simulations of patient-specific aortic dissection

Richard Schussnig[1] | **Malte Rolf-Pissarczyk**[2] | **Kathrin Bäumler**[3] | **Thomas-Peter Fries**[4] | **Gerhard A. Holzapfel**[2,5] | **Martin Kronbichler**[6]

[1]High-Performance Scientific Computing, University of Augsburg, Bavaria, Germany

[2]Institute of Biomechanics, Graz University of Technology, Styria, Austria

[3]Department of Radiology, Stanford University, Stanford, California, USA

[4]Institute of Structural Analysis, Graz University of Technology, Styria, Austria

[5]Department of Structural Engineering, Norwegian University of Science and Technology, Trøndelag, Norway

[6]Applied Numerics, Ruhr University Bochum, North Rhine-Westphalia, Germany

Correspondence
Richard Schussnig, High-Performance Scientific Computing, University of Augsburg, Bavaria, Germany.
Email: richard.schussnig@uni-a.de

Funding information
Graz University of Technology; Bavarian State Ministry of Science and the Arts

Abstract

Modeling an aortic dissection represents a particular challenge from a numerical perspective, especially when it comes to the interaction between solid (aortic wall) and liquid (blood flow). The complexity of patient-specific simulations requires a variety of parameters, modeling assumptions and simplifications that currently hinder their routine use in clinical settings. We present a numerical framework that captures, among other things, the layer-specific anisotropic properties of the aortic wall, the non-Newtonian behavior of blood, patient-specific geometry, and patient-specific flow conditions. We compare hemodynamic indicators and stress measurements in simulations with increasingly complex material models for the vessel tissue ranging from rigid walls to anisotropic hyperelastic materials. We find that for the present geometry and boundary conditions, rigid wall simulations produce different results than fluid–structure interaction simulations. Considering anisotropic fiber contributions in the tissue model, stress measurements in the aortic wall differ, but shear stress-based biomarkers are less affected. In summary, the increasing complexity of the tissue model enables capturing more details. However, an extensive parameter set is also required. Since the simulation results depend on these modeling choices, variations can lead to different recommendations in clinical applications.

KEYWORDS

anisotropy, aortic dissection, computational medicine, fluid–structure interaction, hemodynamics, patient-specific, vascular flow

1 | INTRODUCTION

Aortic dissection is a life-threatening cardiovascular disease characterized by the delamination of the layers of the aortic wall. In an abrupt initial event, tissue layers rupture, creating a cavity and exposing the intralamellar space to blood pressure. This sequence of events results in a secondary flow channel, called the *false lumen*, which is separated from the original *true lumen* by an (initially) thin and flexible tissue layer called the *dissection flap*. The dissection flap may have one or more re-entry tears in addition to the primary entry.

In this context, Abazari et al.[1] verified the anti-hypertensive treatment of type B aortic dissection by modifying the prescribed stroke volume and heart rate, as well as the effects on hemodynamic indicators such as the time-averaged wall shear stress (TAWSS), oscillatory shear index (OSI) and highly oscillatory, low magnitude shear (HOLMES). The effects of surgical treatment with thoracic endovascular repair (TEVAR) on hemodynamics in type B aortic dissections have been studied by Xu et al.,[2] presenting two cases comparing morphological features. Armour et al.[3] performed computational fluid dynamics (CFD) simulations on five individuals with aortic dissection and were able to reproduce and predict the flow field based on patient-specific data. Comparing chronic cases of fully thrombosed, partially thrombosed, and fully perfused aortic dissections with blood flow in a healthy aorta, Moretti et al.[4] found highest false lumen TAWSS and pressure for the fully and partially thrombosed cases. In related work, Kimura et al.[5] investigated hemodynamic and anatomical differences between type B and non-A non-B aortic dissection cases, linking CFD results to late complications. These works underscore the predictive capabilities of computational modeling by employing biomedical markers.

Virtually modifying the aortic geometry can guide further treatment and improve our understanding of the underlying mechanisms. Wan Ab Naim et al.[6] artificially introduced an additional fenestration of the dissection flap in silico. Increased true-to-false lumen fluid exchange leads to decreased pressure differences and, therefore, to a reduced risk of false lumen expansion. Similar results were found by Dillon-Murphy et al.,[7] who also demonstrated good agreement with 4D-flow magnetic resonance imaging (MRI), with a maximum error in the mean flow of 7.6 %. By occluding the entry tear in their computational model along with other variants of the original patient-specific model, Yu et al.[8] revealed that the dissection flap morphology has a dramatic impact on hemodynamics. In this manner, by using CFD, Xu et al.[9] demonstrated the effectiveness of type I hybrid arch repair in non-A non-B aortic dissection, in which hemodynamic indicators returned to baseline after successful intervention. Virtual surgery might also be adopted to assess whether a particular treatment has a high chance of success in the long term, as demonstrated in Li et al.[10] Zhu et al.[11] linked the true-to-false lumen pressure difference to aortic expansion in a longitudinal CFD study on four cases of type A aortic dissection. The authors identify a true-to-false lumen pressure difference of > 5 mmHg as likely leading to unstable aortic growth. Parker et al.[12] considered a significantly larger study cohort of 69 patients. The authors identify proximal thrombosis in the false lumen as the strongest indicator for favorable outcomes because it leads to reduced perfusion in the false lumen and decreased true-to-false lumen pressure differences.

Despite the fact that rigid-wall simulations have been successfully employed to reproduce flow conditions and have shown reasonable, good, or even excellent agreement with clinical data, the extensive literature in this field suggests that some aortic dissection configurations are not suitable for fixed-grid CFD analysis. While in some configurations neglecting the vessel wall compliance leads to acceptable modeling errors, several works have demonstrated the opposite.[13–16] The inclusion of the vessel wall as an elastic object introduces several additional complexities: firstly, blood and tissue exchange momentum and energy, leading to a surface-coupled multi-physics problem; secondly, there are a variety of modeling aspects and related (possibly unknown) parameters that require additional coverage resources; and thirdly, the computational complexity increases greatly, which leads to computing times a factor of 5 to 20 longer at best.

One of the first patient-specific studies on aortic dissection with fluid–structure interaction (FSI) was conducted by Alimohammadi et al.[13] and included a non-Newtonian fluid and an isotropic tissue model of uniform thickness. When comparing FSI and rigid wall CFD models, significant differences in OSI and flow splits were observed, whereas TAWSS was not as affected. In Bonfanti et al.,[17] rigid wall CFD, FSI, and a deformable dissection flap were considered as an extension of the method presented by Bonfanti et al.,[18] which related fluid pressure to normal vessel wall displacements linearly. Similar to Alimohammadi et al.,[13] pressure and flow rates were most affected, while the differences in TAWSS and shear stress-based indicators were not as pronounced. The first FSI model of aortic dissection with two-phase flow was presented by Qiao et al.[14] According to the authors, FSI and multi-phase modeling of the fluid phase have drastic effects on the computational results, for example, up to $\pm 50\,\%$ *relative* difference in WSS between single-phase and two-phase non-Newtonian models. Hemodynamic indicators differed heavily between FSI and rigid wall CFD simulations, despite the fact that a rather stiff linear elastic material was considered. Khannous et al.[16] considered FSI by coupling a non-Newtonian fluid and a linear elastic continuum of constant thickness. Comparing FSI and rigid-wall CFD approaches, the authors document that the CFD simulation tends to overestimate fluid velocities and, therefore, wall shear stress (WSS). Meanwhile, compliance leads in most cases to lumen expansion and, consequently, an increased vessel radius. However, due to the nonlinear coupling of fluid and solid phases, several phenomena such as flow jets or pressure increases triggered by a narrowing of the true or false lumina can occur.

Bäumler et al.[15] presented a patient-specific model of aortic dissection that included a Newtonian fluid and an isotropic hyperelastic solid, as well as boundary conditions tailored to patient data, prestress, and exterior tissue support. Hemodynamic indicators and FSI-specific quantities such as variations in cross-sectional area or flap displacement during the cardiac cycle have been reported for varying dissection flap shear moduli. The numerical framework was then validated via an in vitro model in Zimmermann et al.[19] Flow rates, cross-sectional area, and pressure were compared adopting 4D-flow MRI, 2D cine MRI, 2D PC MRI, and pressure catheter measurements, and showed good agreements for true-to-false lumen flow splits (78/22 % in silico and 73/27 % in vitro), where the computational model overestimates the mean pressure by 15.8 %, velocities and false lumen area expansion (11 % in silico compared to 5 % in vitro). This study highlights that FSI can indeed be used to predict hemodynamics in aortic dissections, but also shows that parameter tuning in such highly complex models is a complicated matter.

Zhu et al.[20] used FSI simulations to investigate repaired type A aortic dissection. A linear elastic material model was employed for the tissue and stent, both of which were coupled to a Newtonian fluid. The authors report significantly increased TAWSS and increased turbulence intensity, but slightly different true-to-false lumen pressure differences when considering the coupled problem. Consequently, the authors conclude that FSI modeling may not be justified compared to rigid-wall CFD in clinical settings. Depending on the study focus, the generalizability of this statement to other cases of aortic dissection remains unclear because the simplified tissue models may not adequately capture the underlying biomechanics.

Continuum mechanics approaches can be fruitfully used to study stresses and strains in tissue, as demonstrated by Wang et al.[21] Based on a case with a nondilated thoracic aorta with type A dissection, a two-layered (intima and adventitia) patient-specific model was constructed that coupled the Holzapfel–Gasser–Ogden model for the tissue and a non-Newtonian fluid including a turbulence model. WSSs in the false lumen were found low in the false lumen and promoted thrombus growth and aortic dilatation, while the maximum von Mises stress in the tissue was found near the bracchiocephalic artery and the stresses in the intima were, on average, higher than those in the adventitia. Unfortunately, the prestress was not taken into account and the fibers were not aligned with the actual *in vivo* microstructure, which potentially influenced the results and slightly reduced the significance of the reported stresses. Although this study combines some of the most advanced modeling techniques, some aspects such as the detailed analysis of stresses in microstructure-related measurements are not yet fully covered.

Within this work, we first present a framework that brings together contributions in this field and documents the central aspects in modeling the vascular system with a focus on aortic dissection. The methods and modeling aspects are applied to a patient-specific case of type B aortic dissection, where, unlike other currently available studies, we consider a combination of: (i) a patient-specific geometry including three tissue layers, namely the combined intima and media, the adventitia, and the dissection flap; (ii) layer-specific tissue models, that is, anisotropic Holzapfel–Gasser–Ogden models with realistic microstructure orientations; (iii) a non-Newtonian rheological model; (iv) patient-specific boundary conditions derived from 4D-flow MRI; (v) viscoelastic exterior tissue support; (vi) prestressed tissue that counteracts diastolic fluid loading; and (vii) aortic root motion prescribed at the inlet. The framework presented is, therefore, one of the most comprehensive currently available. For each case, individual nuances of model complexity and their differences will be highlighted based on hemodynamic indicators such as TAWSS, OSI, HOLMES, true-to-false lumen pressure difference, and volumetric flow rates. Additionally, we report tissue stress measures such as the maximum positive principal stress and the normal and tangential tractions.

The structure of this contribution is outlined as follows: Sections 2 to 5 introduce the numerical framework for analyzing a patient-specific aortic dissection case. This encompasses patient data processing; mesh generation including the implementation of the orientation of the microstructure; tissue and fluid mechanics; and the development of physiological boundary conditions and prestress state. Subsequently, resulting hemodynamic indicators and tissue stress measures are reported in Section 6 considering various levels of model complexity, including a rigid-wall simulation, linear elastic, isotropic hyperelastic, and anisotropic hyperelastic tissue models with distinct material properties per tissue layer coupled to Newtonian or generalized Newtonian fluids. The obtained results and limitations of the study are discussed in Sections 7 and 8, followed by concluding remarks in Section 9.

2 | PATIENT DATA ACQUISITION AND PROCESSING

We consider the case of a 52-year-old man with a residual type B dissection who previously underwent aortic root composite valve graft and hemiarch replacement due to an acute type A aortic dissection. The data set, which includes computed

tomography angiography and 4D-flow MRI data, was acquired eight days postsurgical intervention and originally presented in the work by Bäumler et al.[15] Data processing and use was approved by the corresponding institutional review board (IRB-33403) and the patient confirmed written informed consent.

2.1 | Aortic geometry and mesh construction

The patient-specific model generated is based on the earlier study by Bäumler et al.[15] Briefly, as illustrated in Figure 1, the dissection flap starts at the orifice of the left subclavian artery (LSA) in the aortic arch and extends into the iliac arteries. In each iliac artery, a re-entry tear connects true and false lumina. The LSA is supplied by both true and false lumina, while all other remaining branch vessels are supplied by the true lumen only. Hence, the dissection flap extends from the aortic arch to the interior and exterior left and right iliac arteries at the very bottom of the geometry. This configuration renders computational modeling particularly challenging. Considering only the aortic arch, for example, is troublesome for the present geometry, since severing *both* the true *and* the false lumen is inevitable. Therefore, flow rates at these points must be either assumed or measured to derive meaningful boundary conditions. With the present geometry as shown in Figure 1, we thus avoid introducing a flow ratio between true and false lumina. The intimal surface, in other words the fluid–structure interface, was reconstructed using `SimVascular`[22] and subsequently modified in `MeshMixer`.[23]

Creating the lumen consists of multiple steps.[15] First, segmentations of the true lumen and the combined true and false lumen are created. Then, the true lumen model is expanded outwards by 2 mm in the normal direction. A sequence of Boolean operations then creates a flap with a uniform thickness of 2 mm separating the true and false lumina. Now, extending the luminal surface in the fluid-to-tissue normal direction by 0.8 and 1.2 mm yields the medial and adventitial tissue layers, as illustrated in Figure 2. A similar approach can be taken to create boundary layers in the fluid domain, simply inverting the sweep direction toward the centerline. Such boundary layers in the fluid mesh help capture large gradients in the fluid velocity field. Based on closed surface representations of the individual layers, volumetric mesh generation was then carried out in `Gmsh`.[24] These meshes were subsequently combined by merging matching element nodes. In a final step, the dissection flap was detected by starting from the tissue mesh and then recursively removing tetrahedra on the exterior boundary. This lead to satisfactory results as shown in Figure 2.

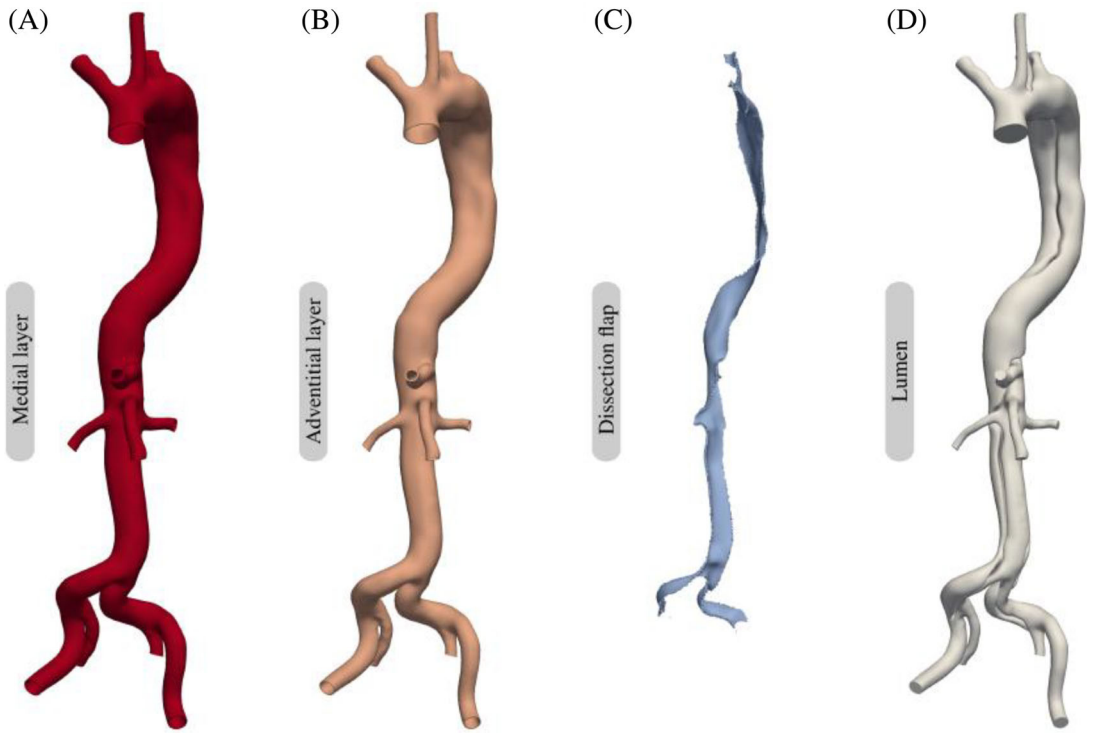

FIGURE 1 Tissue layers and fluid domain: adventitial layer (A; dark red), medial layer (B; peach), dissection flap (C; light blue), and lumen (D; gray).

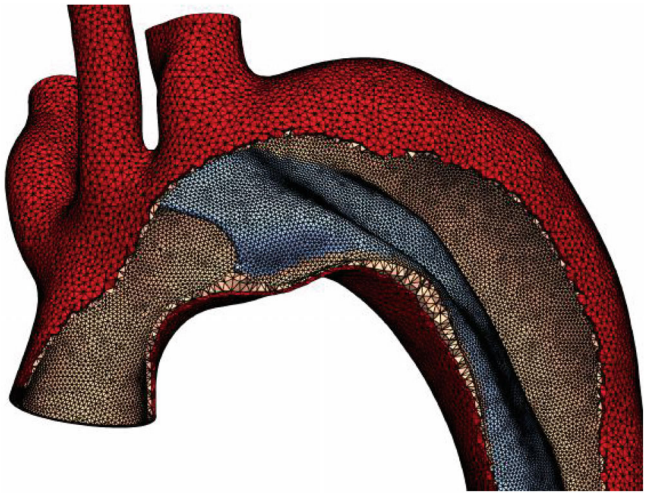

FIGURE 2 Close-up of the finite element mesh in the aortic arch region, showing the cut adventitia (dark red) and media (peach) layers, exposing the dissection flap (light blue) originating at the LSA. The typical separation into true and false lumina is apparent, while this cut shows mainly the false lumen lying anterior.

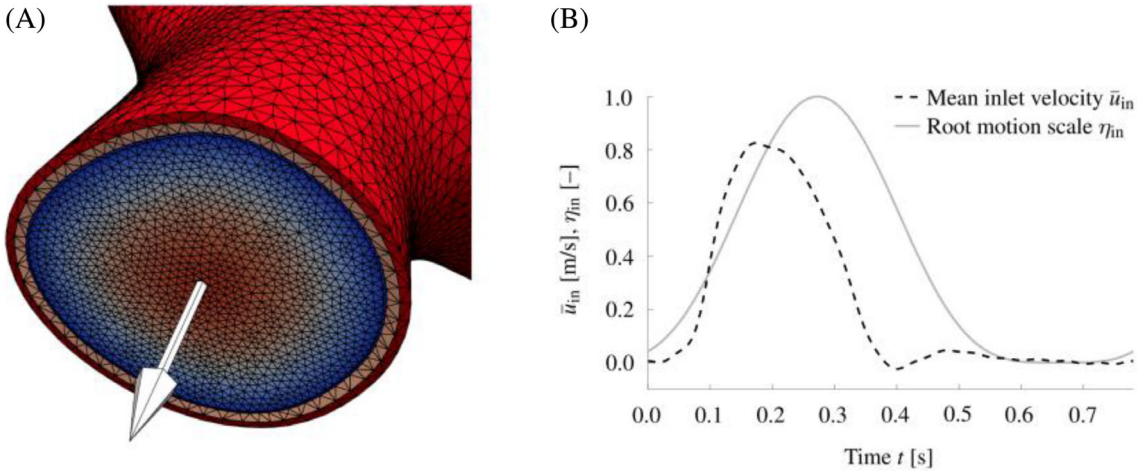

FIGURE 3 Close-up of the aortic root (A) with media (peach) and adventitia (red) tissue layers, color-coded inflow profile, and inverse direction vector; mean inlet velocity $\bar{u}_{in}$ and aortic root motion scale η_{in} (B), as discussed in Section 4.3.

2.2 | Patient-specific flow conditions

In a first step to derive tailored boundary conditions for the fluid problem, patient-specific flow measurements, including 4D-flow MRI data, were conducted by Bäumler et al.[15] The flow rate at the ascending aorta is used to derive a temporal scaling for the inlet condition from the 4D-flow MRI data, as shown in Figure 3, to recover a patient-specific volumetric flow rate. The inlet measures approximately 5.84 cm^2, with a peak systolic flow rate of 28.9 l/ min, an average flow rate of 7.6 l/ min and a period of $T_P = 0.78$ s. The flow rates at each outlet, listed in Table 1, are used to derive suitable Windkessel parameters. These parameters ensure physiological flow splits and pressure levels, as discussion in Section 4.4.

3 | BIOMECHANICAL MODELING

3.1 | Aortic tissue

The dissection flap, along with the medial and adventitial tissue layers are considered three-dimensional, anisotropic, and hyperelastic. They are composed of a ground substance, or a matrix material, reinforced by two families of collagen

TABLE 1 Relative flow rates and Windkessel parameters per outlet approximating flow and pressure data; taken from Bäumler et al.[15]

	q_i (%)	C_i (10^{-10} m^3/Pa)	$R_{p,i}$ (10^7 Pa s/m^3)	$R_{d,i}$ (10^8 Pa s/m^3)
Brachiocephalic trunk	20.2	14.43	4.16	3.74
L. common carotid artery	5.8	4.12	14.48	13.03
L. subclavian artery (TL)	7.6	5.40	11.05	9.95
L. subclavian artery (FL)	5.9	4.19	14.24	12.81
Celiac trunk	12.6	8.95	6.67	6.00
Superior mesenteric artery	4.1	2.91	20.49	18.44
R. renal artery	7.2	5.11	11.67	10.50
L. renal artery	8.4	5.96	10.00	9.00
R. external iliac artery	10.9	7.74	7.71	6.94
R. internal iliac artery	4.5	3.20	18.67	16.80
L. internal iliac artery	9.0	2.63	22.70	20.43
L. external iliac artery	3.7	6.39	9.33	8.40

Note: TL, true lumen; FL, false lumen; L, left; R, right.

fibers.[25] These collagen fibers are the primary load-bearing constituents, particularly in the regime of large strains. They typically exhibit exponential behavior with increased strain. The specific constitutive relation addressed in this study accounts for two fiber families dispersed nonsymmetrically around their respective mean fiber directions, and is based on the work of Holzapfel et al.[25] The implemented tension-compression switch ensures that only fibers under tension contribute to the strain-energy density function. In other words, fibers buckle under compressive load.[26–28] To incorporate this into our numerical framework, we utilize standard relations from continuum mechanics.[26,29] We further define the deformation gradient as $\boldsymbol{F} := \boldsymbol{I} + \nabla_X \boldsymbol{d}$, where $\nabla_X \boldsymbol{d}$ represents the gradient of the displacement field $\boldsymbol{d}$ relative to the Lagrangian reference frame. The balance of linear momentum is then expressed as

$$\rho_s \mathrm{D}_{tt}\boldsymbol{d} - \nabla_X \cdot (\boldsymbol{F}\,\boldsymbol{S}) = \boldsymbol{0} \qquad \text{in} \quad \Omega_s^0. \tag{1}$$

Here, ρ_s denotes the density of the solid in the Lagrangian reference frame Ω_s^0 and $\mathrm{D}_{tt}\boldsymbol{d}$ refers to the material acceleration. We also have neglected body forces for this representation. The explicit expression for the second Piola-Kirchoff stress tensor $\boldsymbol{S}$ is described in the Appendix A. For the discretization in time we consider the generalized-α time integration,[30] while the nonlinear system is solved via Newton's method adopting standard linearizations.[25,26,31,32]

To capture the orientation and dispersion of the fiber families, we use two generalized structure tensors, as described in the Appendix A. The related dispersion parameters a and b as well as the in-plane and out-of-plane angles Φ and Θ facilitate this representation. These angles refer to the local mean fiber directions to the vessel's circumferential direction $\boldsymbol{E}_1$, axial direction $\boldsymbol{E}_2$, and normal direction $\boldsymbol{E}_3$. For our current study, the statistical fiber parameters and shear modulus μ_s for the neo-Hookean ground substance, the bulk modulus (which only weakly enforces incompressibility), and the fiber stiffness and shape parameters k_1 and k_2, are given in Table 2. All tissue parameters except the density $\rho_s = 1200$ kg/m^3 are selected individually for the three layers: dissection flap ($i = 1$), media ($i = 2$), and adventitia ($i = 3$). The shear moduli are $\mu_{s,1} = 62.1$ kPa, $\mu_{s,2} = 62.1$ kPa, and $\mu_{s,3} = 21.6$ kPa, while the bulk moduli $\kappa_{b,i}$ are computed via

$$\kappa_{b,i} := \frac{2(1+\nu_s)}{3(1-2\nu_s)}\ \mu_{s,i}, \quad i = 1, 2, 3, \tag{2}$$

with the Poisson's ratio set to $\nu_s = 0.499$. Note that Equation (2) is only valid for homogeneous isotropic linear elastic materials, but yields high penalty values $\kappa_b \to \infty$ that approach full incompressibility as $\nu_s \to 1/2$. For all tissue layers we consider $k_1 = 1.4$ kPa, $k_2 = 22.1$, while the remaining fiber parameters for the dissection flap and the media are $a_1 = a_2 = 3.62$, $b_1 = b_2 = 34.30$ and $\Phi_1 = \Phi_2 = \pm 27.47°$, for the adventitia, we set $a = 3.08$, $b = 33.20$, and $\Phi_1 = \Phi_2 = \pm 52.88°$,

TABLE 2 Parameter selection for the three tissue layers, namely dissection flap, media, and adventitia, listed for various constitutive models, namely generalized Holzapfel–Gasser–Ogden (gHGO, see Equation (A15)), neo-Hookean (NH), or linear elastic (E90) models.

Tissue model	Parameters
gHGO*	$\mu_{s,1} = \mu_{s,2} = 62.1$ kPa, $\mu_{s,3} = 21.6$ kPa, $\nu_s = 0.499$
gHGO90	gHGO (stiffer dissection flap: $\mu_{s,1} = 90$ kPa)
gHGO120	gHGO (stiffer dissection flap: $\mu_{s,1} = 120$ kPa)
NH	gHGO (without fiber contributions)
E90	$E_1 = E_2 = 89.4$ kPa, $E_3 = 64.4$ kPa, $\nu_s = 0.49$
RWA	None required; rigid wall assumption
***Layer-specific definitions**	
Dissection flap and media	$k_1 = 1.4$ kPa, $k_2 = 22.1$, $a = 3.62$, $b = 34.3$, $\Phi = \pm 27.47°$
Adventitia	$k_1 = 1.4$ kPa, $k_2 = 22.1$, $a = 3.08$, $b = 33.2$, $\Phi = \pm 52.88°$

Note: In all cases the density is $\rho_s = 1200$ kg/m^3.

based on Weisbecker et al.[33] and Rolf-Pissarczyk et al.[34] The mean out-of-plane fiber orientation is controlled with $\Theta = 0°$, yielding the classical helical pattern.

To capture remodeling of the dissection flap, which tends to stiffen over time due to fibrosis,[35] we also considered an increased shear modulus of the dissection flap in the above setting. Material parameters are summarized in Table 2 together with parameters defining simplified models considered for comparison in Section 6.

Finally, we would like to emphasize that the pronounced exponential material response of the adventitia could only be partially reproduced due to numerical challenges in further increasing k_1 and k_2. However, we expect that the implications of this assumption will be minimal because the external tissue support discussed in Section 4.3 limits excessive expansion of the vessel under physiological pressure. Therefore, large strains, where the exponential behavior of the collagen fibers predominantly determines the structural stiffness, are not as relevant here.

3.2 | Blood flow modeling

In the context of the vascular system, blood flow is incompressible, but the fluid can show pronounced non-Newtonian behavior. Under large shear rates, shear-thinning effects become prevalent, while in the quiescent state, higher resistance to relative particle motion can be observed. To incorporate such effects, but simultaneously keep the associated numerical costs low, so-called generalized Newtonian fluid models are among the most viable choices. According to this approach, viscoelastic effects are neglected, but variable viscosity is sufficient to capture the main effects connected to blood flow. Such aspects are particularly important for pathologies such as aortic dissections, stenoses, and aneurysms.[36–39] Comparisons of Newtonian and non-Newtonian models in the patient-specific context have shown that the latter are more consistent with clinical observations,[40] while specifically in aortic dissection, studies using single- and multi-phase (non-)Newtonian fluid models have shown significant differences in shear stress-based indicators.[14,41]

The generalized Newtonian fluid models employed in this work are characterized by a variable viscosity $\mu_f = \mu_f(\dot{\gamma})$, which is a function of the shear rate $\dot{\gamma}$, that is,

$$\dot{\gamma} := 1/2\sqrt{\nabla^s \boldsymbol{u} : \nabla^s \boldsymbol{u}}, \qquad \text{with} \qquad \nabla^s \boldsymbol{u} := 1/2\left(\nabla \boldsymbol{u} + \nabla \boldsymbol{u}^{\mathrm{T}}\right), \tag{3}$$

such that the Cauchy stress tensor can be expressed as

$$\boldsymbol{\sigma}_f := -p\boldsymbol{I} + 2\mu_f \nabla^s \boldsymbol{u}. \tag{4}$$

In the context of vascular flow, prominent choices are the Quemada,[21] Carreau-Yasuda,[13,16,18,42] or the Carreau[31] model, capturing the shear-thinning behavior of blood. The latter rheological law can be expressed as

$$\mu_f(\dot{\gamma}) := \eta_\infty + (\eta_0 - \eta_\infty)\left[1 + (\lambda\dot{\gamma})^2\right]^{\frac{b-1}{2}}, \tag{5}$$

TABLE 3 Parameter combinations considered in Equation (5), resulting in Carreau and Newtonian rheological models.

Rheological model	Parameters
Carreau	$\eta_\infty = 5.13$ mPa s, $\eta_0 = 39.13$ mPa s, $\lambda = 0.9003$ s, $b = 0.3224$
Newtonian	$\mu = 5.13$ mPa s (constant viscosity)

Note: The density is $\rho_f = 1060$ kg/m^3 in both cases.

with upper and lower viscosity limits η_0 and η_∞, and fitting parameters λ and b (the parameter b should not be confused with the concentration parameter introduced above, see also the Appendix A). We can then express the unforced momentum balance and continuity equations on the moving fluid domain Ω_f^t in the Arbitrary Lagrangian–Eulerian (ALE) form as

$$\rho_f \, \partial_t \boldsymbol{u}|_{\tilde{\boldsymbol{x}}} + \rho_f(\boldsymbol{u} - \boldsymbol{u}_m) \cdot \nabla \boldsymbol{u} - 2 \, \nabla \cdot \left(\mu_f \nabla^s \boldsymbol{u}\right) + \nabla p = \boldsymbol{0}, \quad \text{in } \Omega_f^t, \tag{6}$$

$$\nabla \cdot \boldsymbol{u} = 0, \quad \text{in } \Omega_f^t. \tag{7}$$

Here, ρ_f denotes the density of the fluid, $\partial_t \boldsymbol{u}|_{\tilde{\boldsymbol{x}}}$ refers to the ALE time derivative, that is, the time derivative at a moving grid point,[43–45] and $\boldsymbol{u}_m$ denotes the mesh velocity. In the above system (6) and (7), we replace the incompressibility constraint in Equation (7) with a fully consistent Poisson equation in the fluid pressure p, that is,

$$-\Delta p + \nabla \cdot \left[2\nabla^s \boldsymbol{u} \nabla \mu_f - \rho_f(\boldsymbol{u} - \boldsymbol{u}_m) \cdot \nabla \boldsymbol{u}\right] - [\nabla \times (\nabla \times \boldsymbol{u})] \cdot \nabla \mu_f = 0, \qquad \text{in } \Omega_f^t. \tag{8}$$

A finite element approach based on the Equations (6) and (8) in an iteration-free, linearized split-step scheme allows the use of equal-order interpolation and circumvents expensive solves of a saddle-point system.[46] In addition, a streamline-upwind/Petrov–Galerkin method[31,47] is employed to stabilize convective effects, allowing coarser spatial resolution. Regarding the material parameters, the fluid density is set to $\rho_f = 1060$ kg/m^3, and the viscosity limits are set as $\eta_0 = 39.13$ mPa s and $\eta_\infty = 5.13$ mPa s together with $\lambda = 0.9003$ s and $b = 0.3224$ taken from Ranftl et al.[39] Note that these values were deliberately chosen on the upper end of the physiological range (hematocrit of 60%) to highlight existing differences between the Newtonian and the generalized Newtonian models, as the upper and lower viscosity limits cover a larger range in this case. The material parameters are summarized in Table 3, which also lists parameters of a Newtonian model used for comparison in Section 6.

4 | SELECTED TOPICS IN VASCULAR FLUID–STRUCTURE INTERACTION

In addition to the tissue and blood models that capture the constitutive behavior of the involved phases, several other modeling aspects tailored to vascular flow and aortic dissection are essential for reproducing the physiological behavior of the coupled system. For this purpose, the necessary modeling aspects are briefly summarized below, possible pitfalls or shortcomings are highlighted, and the selection of parameters is discussed.

4.1 | Local fiber orientations

To make full use of the anisotropic constitutive relations that are adopted for the aortic tissue, the microstructure orientation needs to be provided in each of the three structural subdomains. Classical approaches are based on solving one or multiple auxiliary Laplace problems with user-defined boundary values to construct smooth fields with gradients approximating, for example, the axial or thickness directions of biological tissues. In more complex scenarios such as bifurcating vessels, aneurysms, the heart, or aortic dissections, standard algorithms frequently fail to deliver satisfactory results. In order to alleviate the problems that arise in such cases, one typically resorts to solving the Laplace problems in suitably selected subdomains of the target geometry and calculates the material orientation per subdomain.[48,49]

Specifically for aortic dissections, prior knowledge of the expected configurations allows for a straightforward approach, avoiding the selection of subdomains and tuning of associated boundary conditions. The key idea in this alternative approach, which was initially proposed in Schussnig et al.,[50] is to combine a single auxiliary Laplace problem solved for the axial direction with a rule-based extrapolation of the normal vector on the intimal surface into the tissue layer by layer with threshold-based averaging. For details on the algorithm and further remarks, we refer the interested reader to our previous work,[31,32] while we restrict ourselves to showcasing the final result obtained for the specific case at hand. Figures 4 and 5 show the circumferential direction $\boldsymbol{E}_1$ and the axial $\boldsymbol{E}_2$ direction. From this we can directly determine $\boldsymbol{E}_3 := \boldsymbol{E}_1 \times \boldsymbol{E}_2$. These directions are then used to evaluate the structure tensors $\boldsymbol{H}_4$ and $\boldsymbol{H}_6$ based on the fiber parameters (see Appendix A).

4.2 | Prestressed reference configurations

The aortic tree is constantly under fluid load and, therefore, the geometry reconstructed from medical image data does not coincide with a stress-free reference configuration as is typically required for a Lagrangian description of the solid. It has been shown that the prestress present in the tissue cannot be neglected in patient-specific scenarios, as it contributes significantly to the overall load-bearing behavior.[15,51–53] To account for these stresses, we adopt the method introduced by Hsu and Bazilevs.[53] In particular, we make a slight modification to the momentum balance of the solid (1) by adding a prestress tensor $\boldsymbol{S}_0$ to the first Piola–Kirchhoff stress $\boldsymbol{P}$, that is,

$$\boldsymbol{P} = \boldsymbol{F}(\boldsymbol{d})[\boldsymbol{S}(\boldsymbol{d}) + \boldsymbol{S}_0(\boldsymbol{d}_0)]. \tag{9}$$

The start-up procedure of the FSI solver thus includes a precursor flow simulation in the rigid lumen to determine the diastolic flow field, which is then used to determine the fluid load involving pressure and viscous forces acting on the structure at the time of image acquisition. We employ an iterative procedure to update $\boldsymbol{d}_0$ in Equation (9) in a load-driven, quasi-stationary approach, combined with a continuation technique[31,32] to facilitate the reconstruction of $\boldsymbol{d}_0$. This, in turn, yields a prestress $\boldsymbol{S}_0(\boldsymbol{d}_0)$ that counterbalances the load, resulting in zero displacements.

The final vector field $\boldsymbol{d}_0$ is shown in Figure 6 and resembles the inflation of the vessel due to diastolic blood pressure. Furthermore, the true-to-false lumen pressure difference at the selected point in the cardiac cycle is reflected in the displacement of the dissection flap. We would like to emphasize that $\boldsymbol{d}_0$ should not be interpreted as an initial

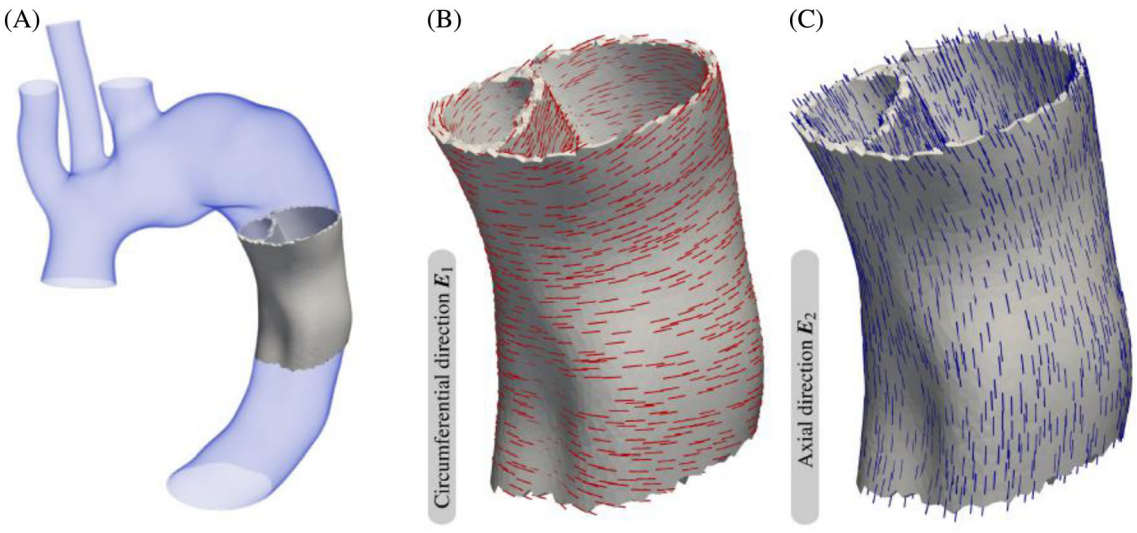

FIGURE 4 Material orientation in a segment of the descending aorta (A): circumferential $\boldsymbol{E}_1$ (B; red) and axial $\boldsymbol{E}_2$ (C; blue) directions. By using threshold-based averaging of the interface normal, we can construct $\boldsymbol{E}_2$ even in the dissection flap, which is in contact with both the true and false lumina.

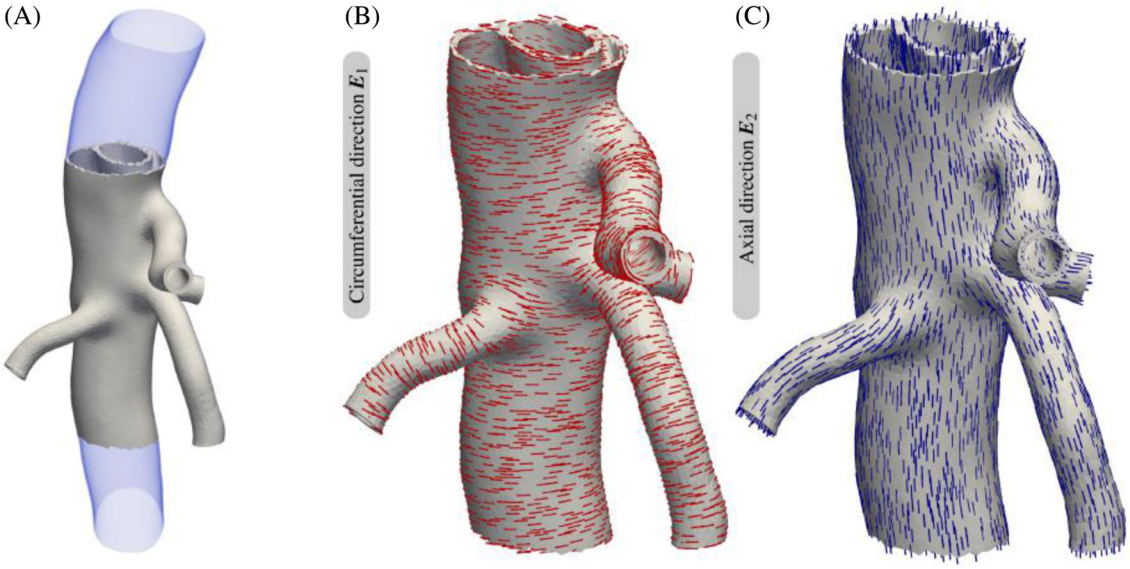

FIGURE 5 Material orientation in a segment of the abdominal aorta (A): circumferential $\boldsymbol{E}_1$ (B; red) and axial $\boldsymbol{E}_2$ (C; blue) directions. The constructed material orientations show a quick and smooth transition for branching vessels.

displacement field in the initial boundary value problem. Instead, it contributes to the momentum balance (1) through the prestress tensor $\boldsymbol{S}_0(\boldsymbol{d}_0)$, as detailed in Equation (9), and remains constant for all time.

In order to stabilize the coupling procedure at the beginning of the FSI simulation, in which vessel compliance is suddenly taken into account and physiological blood pressures are immediately present, a mass-proportional Rayleigh damping of the form $c_m(t)\mathrm{D}_t\boldsymbol{d}$ is considered in the tissue's momentum balance (1). This well-known technique improves temporal stability, coupling convergence speed, prevents finite time blow-up,[54–57] and has proven useful in the vascular regime.[54,55,58,59] The main purpose here is to stabilize the initial 'release' following the prestress computation. Radtke et al.[58] demonstrate that a fixed parameter between $c_m = 0.01$ and $c_m = 0.001$ yields virtually identical results on the cardiac cycle scale under physiological conditions. We therefore choose $c_m = 0.01$ to accelerate convergence, which is scaled down within the first 0.2 s of the first cardiac cycle in the FSI simulation from an initially fairly large value of $c_m = 0.1$.

4.3 | Tethering the aortic tree

The motion of the aortic tree is limited by the exterior tissue, which is modeled by viscoelastic support. To this end, a Robin boundary condition involving the traction vector $\boldsymbol{T}$ in the material configuration (first Piola-Kirchhoff traction vector) is employed, that is,

$$\boldsymbol{T} := \boldsymbol{P}\boldsymbol{N} = -k_e\boldsymbol{d} - c_e\mathrm{D}_t\boldsymbol{d} - p_e, \tag{10}$$

where $\boldsymbol{N}$ denotes the outward normal to the boundary surface. The parameters are considered uniform across the entire vessel exterior as $k_e = 10^7$ N/m^3, $c_e = 10^5$ Ns/m^3, and $p_e = 0$ Pa in a similar range as the related works.[15,60,61] These parameters cause a realistic vessel expansion under physiological blood pressure.

As far as the constraints of the vessel ends are concerned, all of them are fixed except for the aortic root. The motion of the aortic root has a significant influence on the stresses and strains in the ascending aorta, and has therefore been the focus of several studies.[62–68] In addition, high wall stresses correlate with intimal tear locations and areas with pronounced geometrical variations, such as branching vessels, significant tortuosity, or rapid changes in diameter. Aortic root motion has been considered in a patient-specific manner in a number of works,[62,65,69] while others have considered a downward axial systolic root displacement from 10 mm[68] up to 15 mm,[66,67] or a combination of 8.9 mm axial displacement and a 6° clockwise rotation,[63,64] to simplify the rather complex three-dimensional motion.[70] In this study we impose

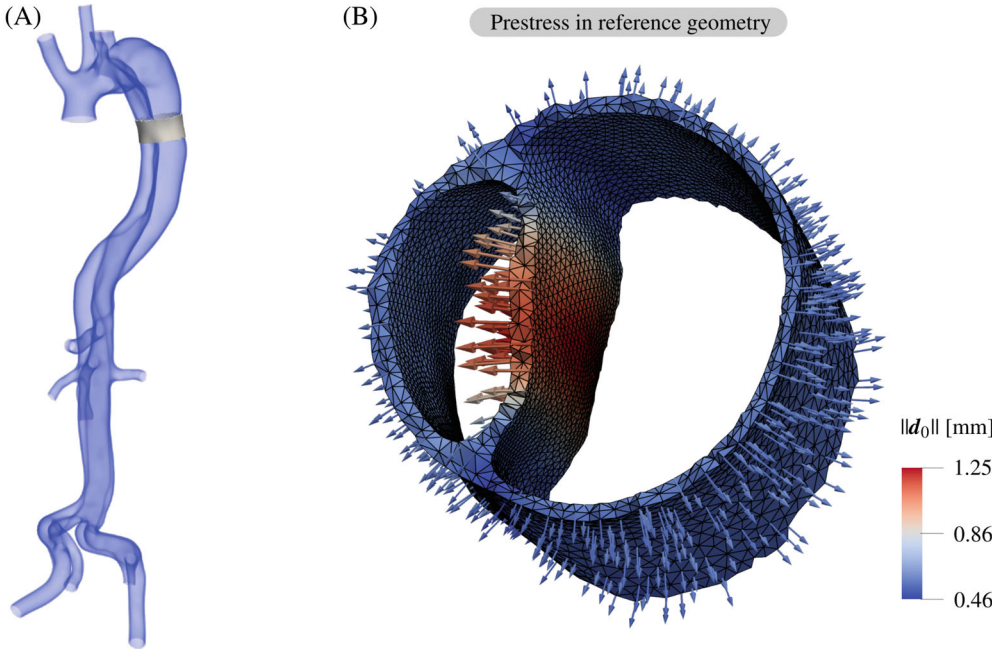

FIGURE 6 The vector field $\boldsymbol{d}_0$ counteracts the diastolic fluid load via $\boldsymbol{S}_0(\boldsymbol{d}_0)$ in a slice located in the descending aorta (A). The coloring takes into account the maximum and minimal values in the slice. The true-to-false lumen pressure difference and the luminal pressure are both reflected in $\boldsymbol{d}_0$ and show an expansion of the vessel and displacement of the dissection flap toward the true lumen (B).

a downward axial displacement, that is, in direction of the vector shown in Figure 3. The maximum amplitude of the displacement equals half the inlet radius R_{in}, that is, $R_{\text{in}}/2 \approx 6.8$ mm lying in the range reported in literature.[70,71] The aortic root undergoes a clockwise rotation of 8° at its base as viewed from the apex, which is within the physiological range.[72] The collective motion of the aortic root combining these two modes begins with a smooth increase over 0.05 s when vessel compliance comes into play. It then scales further according to

$$\eta_{\text{in}} := 1/4\left[1 + \sin\left(\frac{2\pi}{T_p}t - \pi/5\right)\right]^2, \tag{11}$$

with a period of $T_p = 0.78$ s fitting data from Stuber et al.,[72] as depicted in Figure 3.

4.4 | Physiological inflow and outflow conditions

Regarding the inflow boundary condition, we use the scaling technique of Takizawa et al.[73] to construct a quasi-parabolic spatial scale on the noncircular inlet. Due to the aortic root motion, the rescaling procedure is performed at each time step to obtain a patient-specific volumetric flow rate, as shown in Figure 3. At the beginning of the simulation, the boundary condition is gradually increased from a quiescent state over the initial value of 0.1 s. At the remaining outlets i, the flow rates are controlled via three-element Windkessel models that control the mean pressure $p_{c,i}$ at each outlet Γ_i, that is,

$$C_i \frac{\mathrm{d}}{\mathrm{d}t}p_{p,i} + \frac{p_{p,i} - p_{d,i}}{R_{d,i}} = Q_i, \qquad p_{c,i} - p_{p,i} = R_{p,i}Q_i, \tag{12}$$

with the volumetric flow over Γ_i computed as

$$Q_i(\boldsymbol{u}) := \int_{\Gamma_i} \boldsymbol{u} \cdot \boldsymbol{n}\, \mathrm{d}sx, \tag{13}$$

where $\boldsymbol{n}$ is the unit outward normal in the current configuration. In Equation (12) the capacitance C_i incorporates elastic effects of the neglected pipe network, $p_{p,i}$ and $p_{d,i}$ denote proximal and distal pressures, whereas the proximal and distal resistances to the flow, $R_{p,i}$ and $R_{d,i}$, control the amount of backflow by regulating the pressure. The mean pressure $p_{c,i}$ is then enforced via traction conditions on Γ_i.

We adopt the parameter optimization approach from Bäumler et al.[15] and use parameters that are already calibrated for the current data. This ensures errors of less than 10 % in the systolic (p_{sys}) and diastolic (p_{dia}) blood pressure, the pressure amplitude ($p_{\text{sys}} - p_{\text{dia}}$), and the mean pressure, defined as $p_{\text{mean}} = (p_{\text{sys}} + 2\,p_{\text{dia}})/3$. This criterion is fulfilled when the total vascular resistance is set to $R_T = 8.4 \times 10^7$ Pa s/m^3, combined with a total vascular capacitance set to $C_T = 7.1 \times 10^{-9}$ m^3/Pa. The individual outlet's capacitance and proximal and distal resistances are then computed according to $C_i = C_T\, q_i$, $R_{d,i} = k_d\, R_T/q_i$ and $R_{p,i} = (1 - k_d)\, R_T/q_i$, with flow fraction q_i and the setting $k_d = 0.9$ for all outlets.[74,75] The resulting values for each of the outlets are given in the Table 1.

5 | NUMERICAL ASPECTS

The FSI solver and the modeling aspects discussed previously are built upon a consistent splitting scheme[46] and semi-implicit coupling.[31,32] This framework is based on the `deal.II` finite element library[76] and the algebraic multigrid methods provided by Trilinos.[77] Key aspects in this regard are the split-step scheme, which allows added-mass stable coupling in a semi-implicit fashion. Combined with Robin interface coupling conditions and an interface quasi-Newton method,[78] this leads to only two to five iterations in the FSI coupling loop per time step to reach a reduction in the relative error by a factor 10^3, while it also allows iterating only the fluid pressure variable and nonlinear structure solver. Executing the ALE update, fluid momentum balance, and viscosity projection steps once per time step results in a significant reduction in the computational costs.[31,32]

As can be seen from Figure 3, a single boundary layer of 0.25 mm thickness is introduced in the final mesh, while a grid convergence study included grids with up to three boundary layers, and 3.41, 4.21, and 5.11 million finite elements. When comparing flow rates and pressures at each of the outlets, sufficient agreement (with differences lower than 7 %) between coarse and fine mesh results were found. We attribute this agreement to the following factors: (i) the boundary layer mesh, which offers enhanced accuracy over uniform meshes and aligns closely with models including turbulence in the context of aortic dissection[2,79]; (ii) the multi-layer tissue model, which already employs element sizes around 1 mm ensuring the media and adventitia are accurately represented even in the coarsest grid; and (iii) the relatively smooth solution fields, resulting from the lack of sharp re-entrant corners. The time step size was chosen adaptively to ensure accuracy and stability of the semi-implicit scheme. This results in time step sizes ranging from 0.1 ms during systole up to 1 ms, which is the maximum time step size enforced. For the present case, the first two cardiac cycles are considered as precursor flow simulation (rigid wall flow simulation), since the diastolic pressure and an approximately periodic solution is already reached. Thereafter, the diastolic load and corresponding prestress field are computed, to finally couple the fluid and solid fields for five cardiac cycles. The results are reported for the seventh cardiac cycle, where a periodic solution is reached.

To investigate the effects of various modeling options, we aim to compare hemodynamic and tissue indicators in Section 6. The starting point is the model that considers three tissue layers of fiber-reinforced anisotropic material, as shown in Section 3.1, which we subsequently call the generalized Holzapfel–Gasser–Ogden model (gHGO).[25] Additionally, we employ models with a stiffened dissection flap, considering $\mu_{s,1} = 90$ kPa (gHGO90) and $\mu_{s,1} = 120$ kPa (gHGO120), which aims to capture remodeling of the dissected flap and corresponding stiffening over time. In a simplifying assumption, we also adopt an isotropic, nearly incompressible neo-Hookean model (NH), omitting the fiber contributions compared to the baseline gHGO model. Further simplification leads to a linear model, which ignores finite strains altogether and assumes isotropic, elastic material behavior, referred to as E90. The simplified models, NH and E90, do not reflect the exponential stress-strain relationship inherent in aortic tissue. However, from a computational perspective, they are appealing. The operator evaluation is more cost-effective, and the latter E90 model results in a linear problem. Further, we include a simulation based on a rigid wall assumption (and zero aortic root motion) in our studies, referred to as RWA, which adopts a generalized Newtonian fluid flow simulation neglecting vessel compliance (apart from the Windkessel models at the outlets). Depending on the study target, these simplified models might be attractive choices as well. The material parameters of the tissue for each of the models are summarized in Table 2. Concerning the choice of rheological law, we always pair the nonlinear tissue models with a Carreau fluid, but reduce the complexity when combined with the linear elastic model, E90, leading to a Newtonian fluid. Fluid parameters are summarized

TABLE 4 Aortic dissection models combining tissue and rheological models according to Tables 2 and 3.

Aortic dissection model	Tissue model	Rheological model	Root motion
gHGO	gHGO	Carreau	✓
gHGO90	gHGO90	Carreau	✓
gHGO120	gHGO120	Carreau	✓
NH	NH	Carreau	✓
E90	E90	Newtonian	✓
RWA	RWA (none)	Carreau	×

Note: All except the RWA model account for aortic root motion, as discussed in Section 2.2.

in Table 3, and the resulting models are listed in Table 4. Contrary to the tissue models, execution times for Newtonian and non-Newtonian fluid models are rather similar, since merely an explicit viscosity projection step with a lumped mass matrix is solved additionally.[31,46]

This model selection therefore enables the comparison of material models of different complexity (gHGO, NH, E90, and RWA), investigating the effects of increased flap stiffness (gHGO, gHGO90, and gHGO120) and covers models of low, medium, and high complexity (RWA, NH, and gHGO). However, keep in mind that E90 and RWA comparisons are about more than a single model change. This is because the E90 model follows the linear material behavior of blood and tissue, and the latter takes into account a rigid domain, that is, a zero movement of the geometry.

6 | RESULTS

6.1 | Dissection flap displacement

First, we compare point-wise solutions obtained with the different models. Figure 7 shows point A located on the proximal dissection flap in the true lumen. Here we report the displacement $\boldsymbol{d}$ in the seventh cardiac cycle. To relate the transients to cardiac output, the inflow and aortic root motion scales $\bar{u}_{\text{in}}$ and η_{in} are added in scaled form. If we adopt the material parameters as described, we measure a displacement of up to 3.5 mm for gHGO and NH, which produce almost identical results in this simplified norm. Of course, by stiffening the dissection flap, the observed displacement is reduced to 2.5 and 1.7 mm for the gHGO90 and gHGO120 models, respectively. The linear elastic model leads to 2.3 mm. In all approaches considered, the peak displacement at point A is expected to occur shortly after peak systolic inflow. In the diastolic phase, the motion of the dissection flap is reversed, causing the true lumen to narrow and reach its initial position. Notably, the maximum deformation of 3.5 mm computed with the gHGO and NH models underestimates the clinically observed displacements of the dissection flap, which reach 8.7 mm.[15] We attribute these discrepancies to the combination of a possible overestimated dissection flap thickness and overly smooth transition from the outer vessel wall to the dissection flap, which provides additional support to the dissection flap. Both are due to challenges related to construction of the boundary layer mesh. To counteract these two effects and achieve the displacements of the dissection flap observed *in vivo*, one could adjust the material parameters of the tissue, specifically by lowering the shear modulus in the dissection flap below the selected parameters.[80] Additionally, unlike previous work,[15] the dissection flap contains a prestress, which is also expected to impact the results.

6.2 | Volumetric flow rates

Volumetric flow rates and false lumen perfusion are important hemodynamic indicators in aortic dissection. To this end, we evaluate the true and false lumen flow rates Q_i according to Equation (13) through five selected cross sections along the aorta. The selected points for assessing cross-sectional flow are at the levels of the LSA, the pulmonary artery (PA), the left ventricle (LV), proximal to the celiac trunk (CT), and in the abdominal aorta (ABD). Figure 8 combines a snapshot of the velocity at peak systolic flow in the cross sections with flow rates for the true and false lumina reported for the entire cardiac cycle. The snapshot shows results obtained via the baseline gHGO model at peak systole as indicated by the inflow scale, with the increased flow through the true lumen and corresponding higher velocities easily identified. We compare different levels of model complexity using the discussed models and parameters, as listed in Tables 2 and 3,

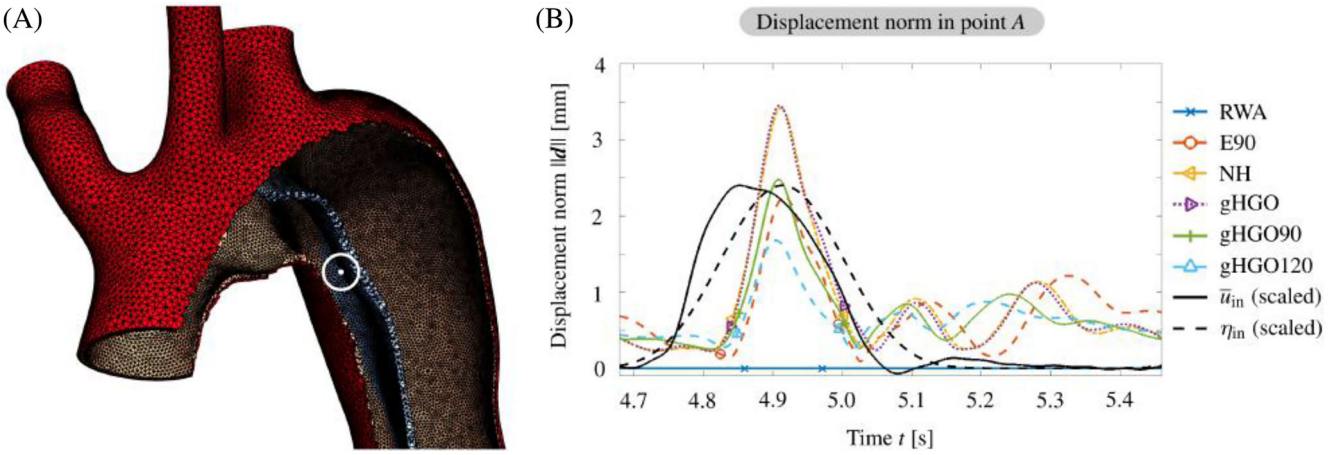

FIGURE 7 Displacement $\boldsymbol{d}$ at point A ($\odot$), located in the descending aorta at the proximal end of the dissection flap in the true lumen, relative to the inflow and aortic root motion scales $\bar{u}_{in}$ and η_{in}. The gHGO and NH models provide similar results, while stiffening of the dissection flap (light blue and light green) leads to a reduced maximum amplitude. Peak displacements occur at peak systole, while the dissection flap exhibits oscillatory motion during diastole.

and additionally include simulation results from Bäumler et al.[15] The latter are referred to as E20*, E50*, E100*, and E800*, and are based on a model coupling an incompressible Newtonian fluid and a nearly incompressible neo-Hookean solid. These simulations consider a Poisson's ratio of $\nu_s = 0.49$ and a Young's modulus of $E = 800$ kPa in the outer arterial wall and $E = 20, 50, 100, 800$ kPa for the dissection flap, where the shear rate is then deduced from $\mu_s = (1 + \nu_s)E/2$. The boundary conditions are chosen to be almost identical, only the inflow profile and the tethering of the vessel tree or exterior tissue support are slightly adjusted compared to the present work.

In general, the waveforms show good agreement. However, variations occur in simulations that consider exceptionally low or high stiffness or completely neglect vessel compliance. The RWA simulation differs notably from the E800*, which corresponds to an FSI simulation with small deformation of the dissection flap. However, this small deformation is already enough to significantly influence the flow split between between true and false lumina. In systole, the results obtained with the different approaches agree well, while in diastole, the simulations with lower stiffness show pronounced fluctuations and increased transient behavior. The gHGO models with varying dissection flap stiffness and the neo-Hookean model provide similar results in this comparison without significantly changing the results.

Figure 8 also presents flow rates derived from MRI data. When comparing the in silico results with the MRI measurements, we observe discrepancies similar to those in the previous study.[15] Most notably, the peak systolic flow in the proximal true lumen is underestimated, while reversed flow in the distal false lumen is observed. Despite the various differences in the modeling approaches in the original work and the current study, the observed overall trends are similar, but no in silico approach is able to reproduce the *in vivo* flow field and conditions. We posit that these differences are at least partly due to the simplified inflow velocity profile used. While the quasi-parabolic shape considered in this study is consistent with the volumetric flow rate, the inflow profile found *in vivo* is certainly more complex.

6.3 | True-to-false lumen pressure differences

A second crucial biomarker is the pressure difference between the true and false lumina. A nonzero true-to-false lumen pressure difference may contribute to the progression of dissection by creating an imbalance in surface loads on the dissection flap, thereby leading to its deformation. Continuous movement caused by alternating positive and negative pressure gradients across the dissection flap could also result in collapse of the true lumen. This is another life-threatening complication in aortic dissection, which potentially leads to malperfusion of vessels supplied solely by the true lumen. In this context, Zhu et al.[11] identified a true-to-false lumen pressure difference of > 5 mmHg as likely leading to unstable aortic growth in a longitudinal study, which we consider here as a potential threshold value. The pressure difference between the true and false lumina is calculated by determining the difference of the integral means over the sections of

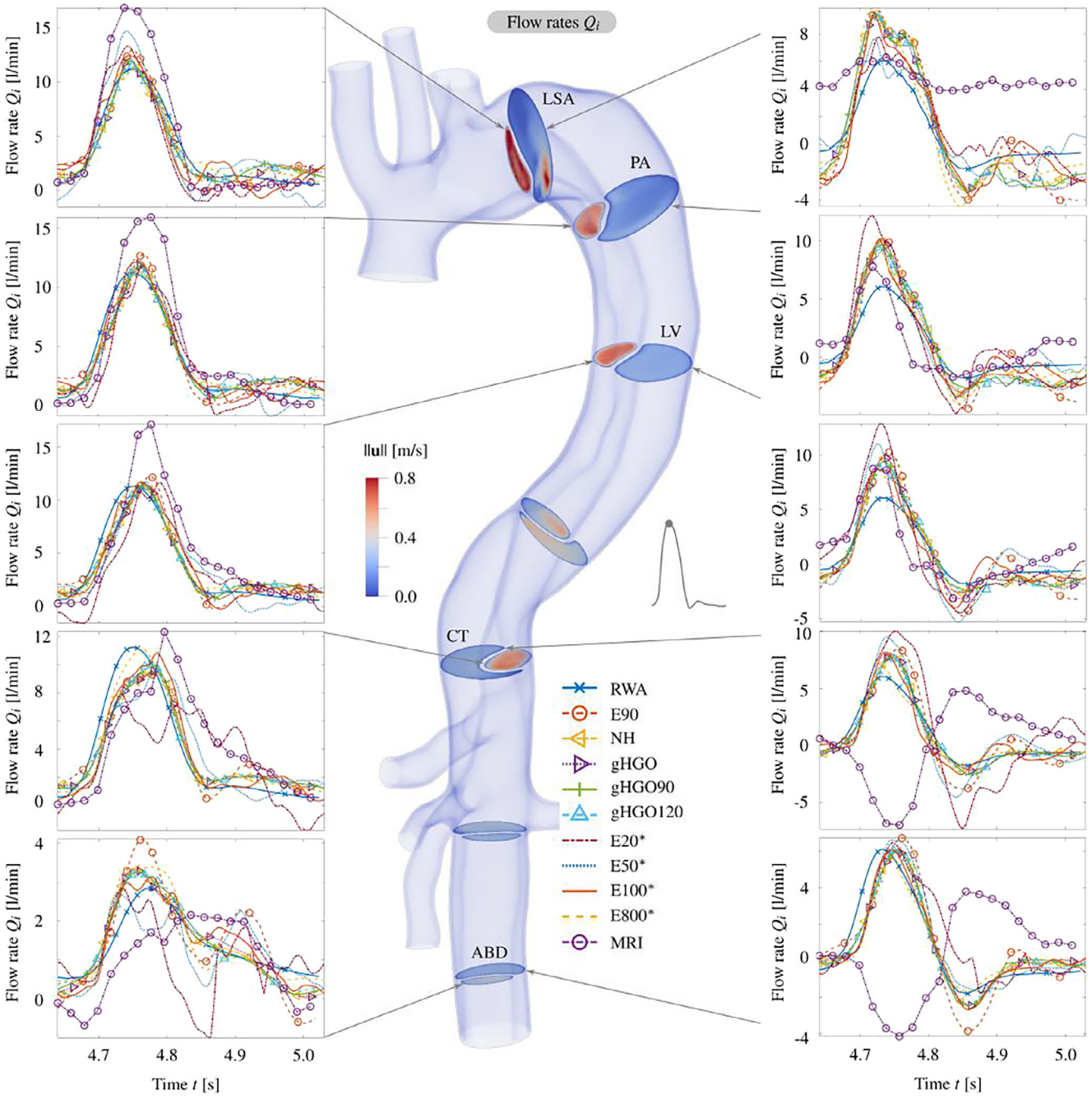

FIGURE 8 Snapshot of the velocity in the aorta considering the gHGO model at peak systole and flow rates over the cardiac cycle in the true lumen (left) and false lumen (right). Models based on a RWA, FSI approaches of increasing complexity (E90 to gHGO) or increased dissection flap stiffness (gHGO to gHGO120) are compared with results from Bäumler et al.[15] (E20⋆ to E800⋆). Extreme values of tissue stiffness affect the results, while most simulations produce similar transients showing that the perfusion and related velocities are higher in the true lumen than in the false lumen.

the true and false lumina within a slice, denoted as Γ_{TL} and Γ_{FL}, yielding

$$\Delta p_{\mathrm{TL/FL}} := \frac{\int_{\Gamma_{\mathrm{TL}}} p \, \mathrm{d}s x}{\int_{\Gamma_{\mathrm{TL}}} 1 \, \mathrm{d}s x} - \frac{\int_{\Gamma_{\mathrm{FL}}} p \, \mathrm{d}s x}{\int_{\Gamma_{\mathrm{FL}}} 1 \, \mathrm{d}s x}. \tag{14}$$

In Figure 9, we present the pressure in the selected slices (LSA, PA, LV, CT, and ABD) as determined by the baseline gHGO model at peak systole. We also display the true-to-false lumen pressure difference over the cardiac cycle

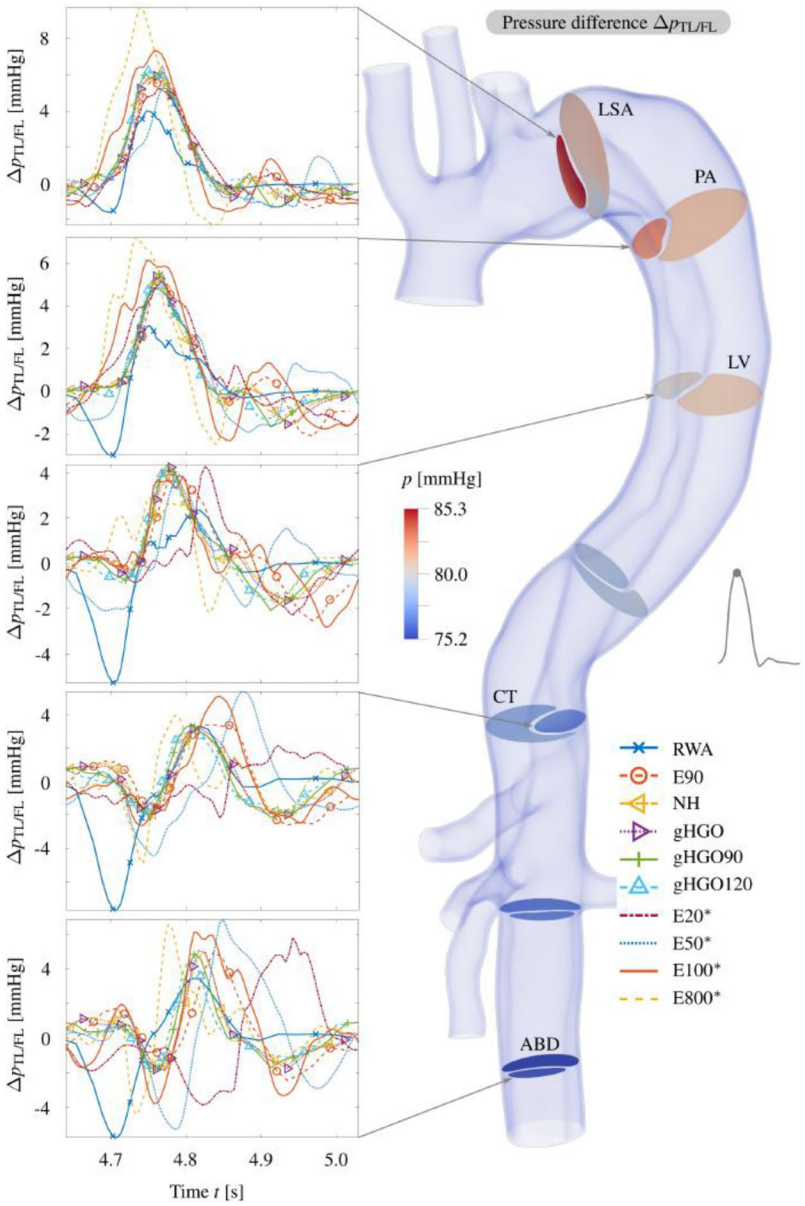

FIGURE 9 Snapshot of the pressure in the aorta considering the gHGO model at peak systole and the true-to-false lumen pressure difference according to Equation (14) for selected cross sections. Models based on a RWA, FSI approaches of increasing complexity (E90 to gHGO) or increased dissection flap stiffness (gHGO to gHGO120) are compared to results from Bäumler et al.[15] (E20⋆ to E800⋆). Model simplifications and modified stiffness parameters lead to different results. Deviations from the literature are due to the non-Newtonian fluid, viscoelastic support, and differing tissue parameters.

and compare with the simplified approaches and data from Bäumler et al.[15] At peak systole, a positive gradient across the dissection flap is observed, which reverts during diastole depending on the tissue parameters. Most notable are again the differences between the gHGO, RWA, and E800⋆ models. The RWA model shows even a negative true-to-false lumen pressure difference in early systole and a decreased or similar positive true-to-false lumen pressure difference in late systole and the diastolic phase, while the E800⋆ model features an elevated true-to-false lumen pressure gradient in systole.

When considering FSI with hyperelastic tissue properties, all approaches result in comparable true-to-false lumen pressure differences at LSA, exhibiting slightly negative values during diastole and reaching maximum positive peak values during systole. The peak of the positive pressure difference is less pronounced in the distal regions of the aorta, where the single peak positive value at systole in the proximal regions slowly transitions into a slight positive peak and

two negative peaks in the abdominal region. In general, the observations show that: (i) the simplified assumption of a rigid vessel leads to significantly different outcomes in the current case; (ii) the linear elastic model (combined with a generalized Newtonian fluid) exhibits discrepancies in the distal regions, particularly during diastole, while the other nonlinear models largely agree. As for the reference results from the literature, we see that E50⋆ and E100⋆ models are most consistent with the results obtained with the current framework as similar tissue parameters were employed to obtain these reference values. We attribute the remaining differences to the non-Newtonian fluid model used here and the viscoelastic support.

For completeness and to further quantify these observations in relation to the true-to-false lumen pressure difference, Table 5 lists the differences in the maximum and minimum $\Delta p_{\mathrm{TL/FL}}$ for each model over the entire seventh cardiac cycle, while similar data for the remaining slices can be found in Appendix B in Tables B1–B4. Taking the highlighted gHGO model as reference, we can thus verify from the upper right half of Table 5 that the gHGO and gHGO120 models provide similar minimum true-to-false lumen pressure differences, higher than the remaining models. Therefore, one can conclude that the predictions using the gHGO and gHGO120 models indicate a lower probability of false lumen expansion at the cross section at LV level because the overpressure in the false lumen, resulting in a negative $\Delta p_{\mathrm{TL/FL}}$, is smaller in absolute terms compared to the other simulations. The difference to the NH is minor in this norm, while E90 and especially the RWA models deliver significantly different values from the gHGO reference, but one has to keep in mind that the evolution of the true-to-false lumen pressure difference over time is lost in this procedure, and other models that provide similar maximum or minimum values may actually differ significantly in their evolution over time.

Examination of the maximum true-to-false lumen pressure difference in the cross section at the LV level (lower left half of Table 5), we see that increasingly stiffer FSI models and the RWA model tend to predict smaller maximum true-to-false lumen pressure differences. Note that the evolution of the pressure over time is lost again. The trend of increasing negative pressure peak in the beginning systole with increased stiffness is also visible in Tables B1 to B4 (Appendix B) and manifests itself in a high negative value in row RWA and column gHGO (gHGO value minus RWA value in mmHg: LSA: 0.67, PA: 1.46, LV: 3.63, CT: 5.51, ABD: 3.86) as well as in a high positive value in the gHGO row and E800⋆ column (gHGO value minus E800⋆ value in mmHg: LSA: 1.37, PA: 0.95, LV: 0.55, CT: 2.72, ABD: 2.55).

However, the tables are not solely based on comparisons to the gHGO reference to enable cross comparisons between the individual models. For example, we can easily compare the RWA model to the remaining ones looking at the first row and column of Table 5: the first row shows that the RWA model provides the lowest minimum true-to-false lumen pressure difference in the cross section at the CT level of all models, while the first column indicates the lowest maximum $\Delta p_{\mathrm{TL/FL}}$ compared to all models in this cross section.

TABLE 5 Discrepancy between predictions of the true-to-false lumen pressure differences in the cross section at the LV level in mmHg, determined by the different models: differences in maximum (lower left half) and minimum (upper right half) $\Delta p_{\mathrm{TL/FL}}$ over the entire seventh pulse cycle.

	RWA	E90	NH	gHGO	gHGO90	gHGO120	E20⋆	E50⋆	E100⋆	E800⋆
RWA	+0.00	−2.72	−3.57	−3.63	−3.18	−3.63	−2.95	−3.16	−2.45	−3.08
E90	+1.64	+0.00	−0.85	−0.91	−0.46	−0.91	−0.23	−0.44	+0.27	−0.36
NH	+1.68	+0.04	+0.00	−0.06	+0.39	−0.07	+0.61	+0.41	+1.12	+0.49
gHGO	+1.87	+0.23	+0.19	+0.00	+0.45	−0.00	+0.67	+0.47	+1.18	+0.55
gHGO90	+1.99	+0.35	+0.31	+0.12	+0.00	−0.46	+0.22	+0.02	+0.73	+0.10
gHGO120	+1.74	+0.10	+0.06	−0.13	−0.26	+0.00	+0.68	+0.47	+1.18	+0.55
E20⋆	+1.92	+0.27	+0.24	+0.05	−0.08	+0.18	+0.00	−0.21	+0.51	−0.12
E50⋆	+1.50	−0.14	−0.18	−0.37	−0.49	−0.24	−0.42	+0.00	+0.71	+0.08
E100⋆	+1.48	−0.16	−0.20	−0.39	−0.51	−0.26	−0.44	−0.02	+0.00	−0.63
E800⋆	+0.54	−1.10	−1.14	−1.33	−1.45	−1.19	−1.37	−0.96	−0.94	+0.00

Note: The difference between row *i* and column *j* is computed as the value from model in row *i* minus the value from model in column *j*.

6.4 | Rheology

Local hemodynamics, flow splits, and pressure differences between true and false lumina, among other influencing factors, have a major effect on thrombus formation in aortic dissection.[12] Complete false lumen thrombosis can promote remodeling of the aorta and lead to favorable long-term outcomes. Although thrombus modeling in aortic dissection has been explored[81,82] and the current framework incorporates a kinematics-based thrombus formation model,[83,84] we decided not to adopt this complicated modeling approach due to the absence of a thrombus in the false lumen *in vivo*. Similar to the previous sections, Figure 10 shows a snapshot of the dynamic viscosity μ_f at peak systole, while also reporting on the integral-average viscosities in the true and false lumen parts of each cross section.

Although large velocity gradients near the vessel wall result in high shear rates with viscosities near the Newtonian limit, we observe increased viscosity at the centers of both the true and the false lumen. Depending on the flow rate and the resulting velocity gradients, the apparent viscosity varies over the course of the cardiac cycle, where the larger hydraulic radius of the false lumen combined with the lower flow rate lead to an increase in viscosity. In the proximal regions and especially during systole, the integral mean of the viscosity approaches the Newtonian limit due to the recirculatory flow in the entry tear region. However, due to the low shear rates in the lumen centers, the integral mean over each of the cross sections is higher than the Newtonian limit. Starting in the proximal descending aorta, where the diameter of the false lumen increases, and continuing into the thoracic aorta, we observe lower shear rates and consequently higher viscosities. Higher viscosity indicates increased shear resistance, further reducing the flow rate in the false lumen. This continues until equilibrium is reached where the hydraulic pressure driving the fluid through the false lumen equals the additional energy lost due to increased viscosity.

Naturally, the simplified E90 model shows a constant viscosity of $\mu_f = 5.13$ mPa s since we consider a Newtonian fluid in this case, while the remaining models consider a Carreau fluid, see Table 4. The integral means in the false lumen of the NH and gHGO models with increasing stiffness in the dissection flap (gHGO, gHGO90, and gHGO120) exhibit differences during the diastolic phase. This is when flow rates and shear rates decrease, leading to a subsequent increase in viscosity. Similar results are obtained during systole and within the true lumen. However, particularly high values of viscosity in the false lumen and the resulting reduced flow can influence the onset of false lumen thrombosis. The differences observed here could therefore actually impact the model response over time. This aspect may then further influence thrombus growth and related aortic remodeling, potentially greatly affecting hemodynamics and the response of the entire system. Finally, we would like to point out that most of the transients presented in Figure 10 show periodic results, but this does not apply to the cross section at the pulmonary artery level. This is because the data range does not perfectly cover the entire cardiac cycle and there may be nonperiodic solution components that have not yet faded in the first seven pulse cycles or are periodic over multiple cycles.

6.5 | Shear stress-based indicators

The TAWSS is an important hemodynamic indicator that is the integral mean of the absolute shear stress over cardiac cycle i of length T_p, that is,

$$\text{TAWSS} := 1/T_p \int_{(i-1)T_p}^{iT_p} |\boldsymbol{\tau}| \, \mathrm{d}t, \qquad \text{with} \quad \boldsymbol{\tau} := 2\mu_f \boldsymbol{n} \cdot \nabla^s \boldsymbol{u} - 2\mu_f \left[\boldsymbol{n} \cdot \left(\boldsymbol{n} \cdot \nabla^s \boldsymbol{u}\right)\right] \boldsymbol{n}. \tag{15}$$

Tissue exposed to elevated TAWSS for an extended period has a higher likelihood of rupture,[85,86] whereas low TAWSS is likely to promote risk of endothelial cell degeneration and serves as a key activator in thrombus formation.[81–83] The TAWSS is evaluated for the seventh cardiac cycle adopting the RWA, E90, and gHGO models and compared in Figure 11. In all three models, areas of elevated TAWSS are found in the ascending aorta, in the true luminal arch region, near branching vessels, and in the iliac arteries due to their pronounced curvature. The RWA simulation neglecting vessel compliance yields notably elevated peak TAWSS values in an extended area with an increased TAWSS value of > 2.5 Pa. Areas of low TAWSS < 0.2 Pa are mainly found in the false lumen, which is due to its low flow rate and large radius. Interestingly, the RWA model shows lower TAWSS in the false lumen, while the FSI models E90 and gHGO show slightly increased TAWSS in the false lumen, presumably caused by the wall motion due to pressure variations over the cardiac cycle.

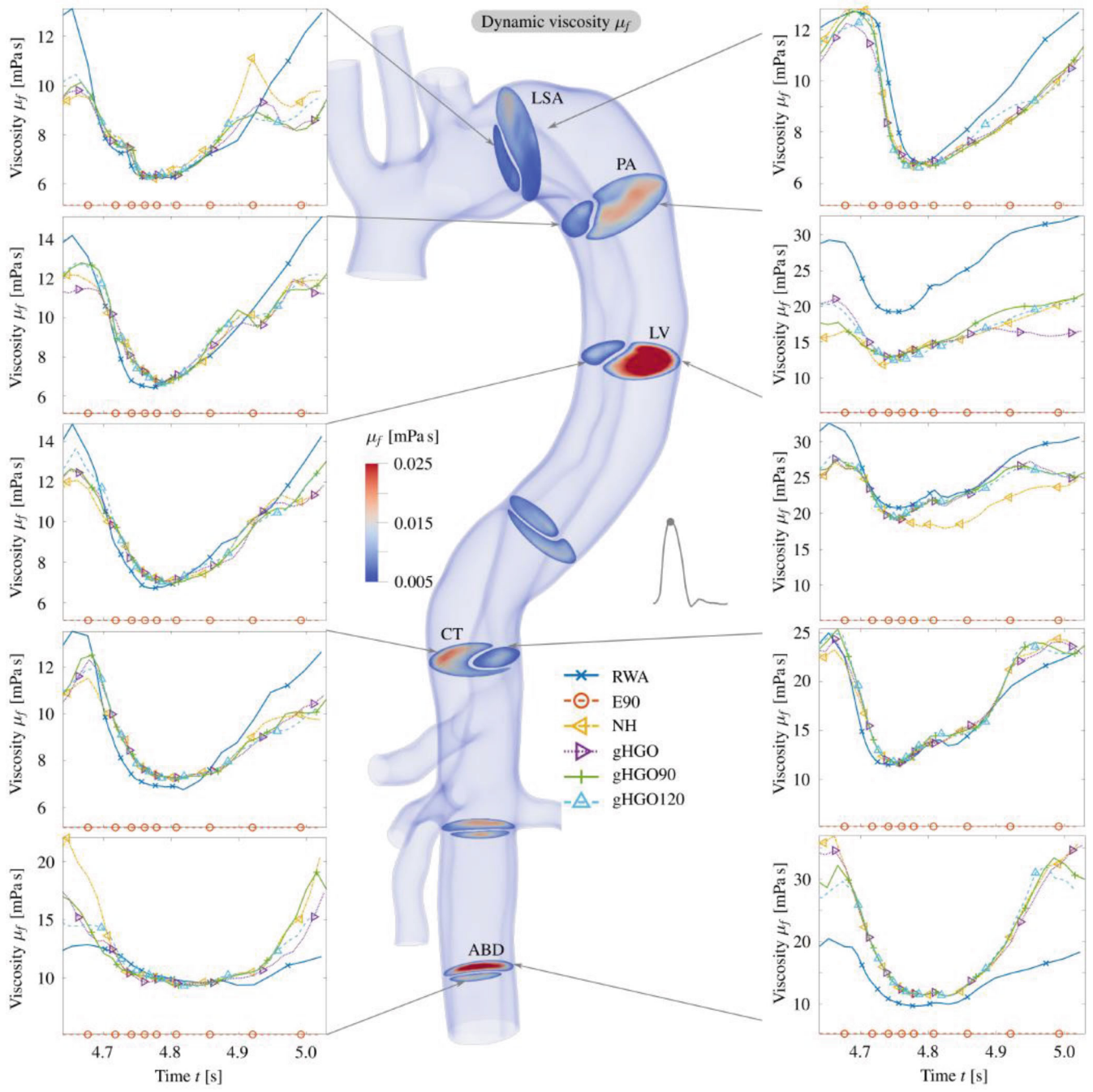

FIGURE 10 The 3D model shows a snapshot of the dynamic viscosity μ_f in the aorta for the gHGO model at peak systole. Transients during the cardiac cycle are reported separately for the true lumen (left) and the false lumen (right) for all material models. E90 considers a Newtonian fluid, while the remaining models apply a Carreau law. All nonlinear tissue models produce similar results, except for the proximal false lumen. High viscosities occur in diastole, while the Newtonian limit is reached in systole. Discrepancies between models might impact other predictions such as thrombus formation or hemodynamic indicators and are therefore considered relevant.

Related to the TAWSS, the OSI is defined as

$$\mathrm{OSI} := 1/2 - \frac{\left| 1/T_p \int_{(i-1)T_p}^{iT_p} \boldsymbol{\tau} \, \mathrm{d}t \right|}{2 \, \mathrm{TAWSS}}, \tag{16}$$

with values between 0 and 0.5 indicate the orientation of the shear stress acting on the lumen wall. The zero OSI refers to regions where the orientation of the WSS remains unchanged throughout the cardiac cycle, while the OSI for fully

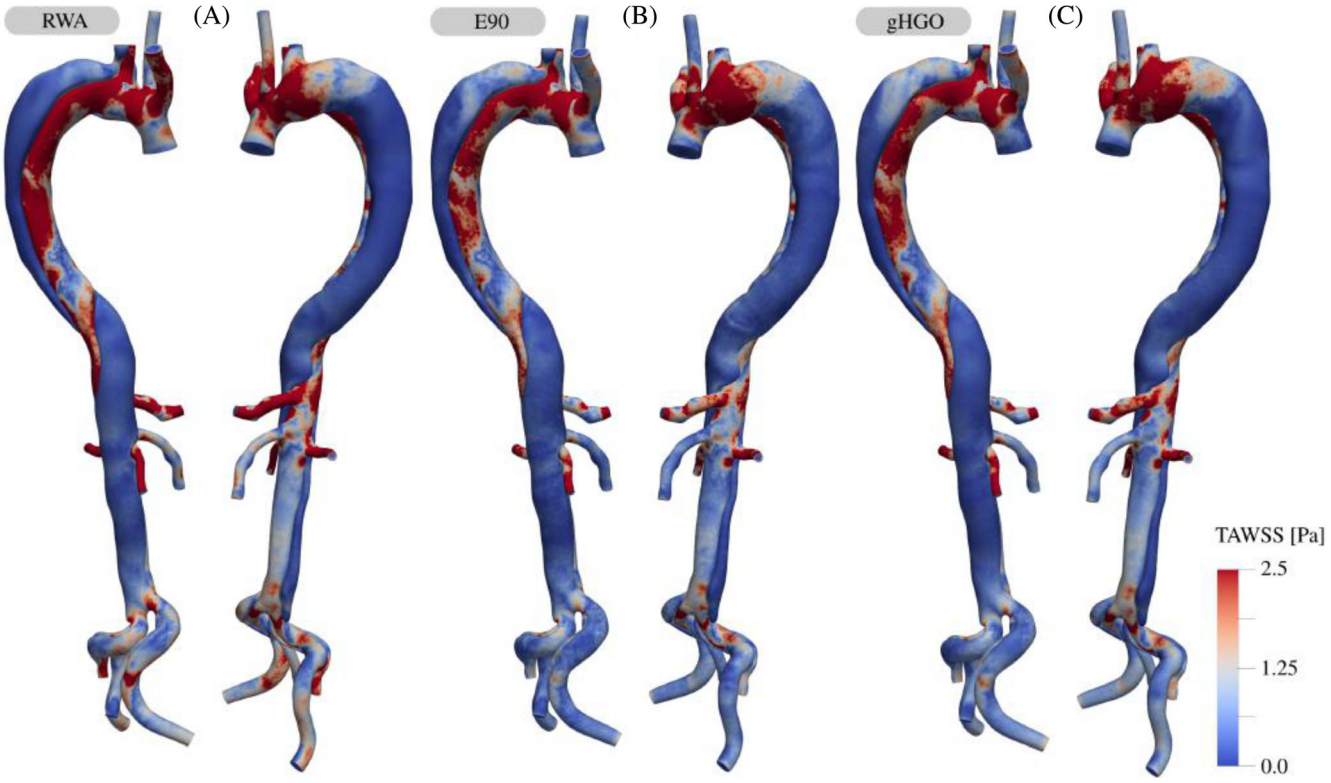

FIGURE 11 TAWSS integrated over the seventh cardiac cycle, determined with the RWA (A), E90 (B), and gHGO (C) models. High TAWSS values are found in the arch region, at branching vessels, and true lumen. The false lumen has a low TAWSS for all models. The simulation assuming rigid walls results in higher peak values and an expanded area of high TAWSS, while the low TAWSS areas are also more pronounced. Note that the legend in (C) also applies to (A) and (B).

oscillating shear stresses that perfectly reverse direction at each time step reaches 0.5. The OSI, which acts on the endothelial cells, is computed over the seventh cardiac cycle using the RWA, E90, and gHGO models. This is illustrated in Figure 12, where areas with high OSI correspond to areas of recirculatory flow that exhibit unstable and complex flow patterns. This is the case both in the true and the false lumen, with the latter featuring extensive areas of an OSI close to 0.5. Clear differences can be seen between all models considered, but the general patterns agree well. A relative measure of the differences between the models, as discussed in various places in the literature,[1,14] would show high relative differences in OSI. For brevity, we have omitted such comparisons because Figure 12 suggests that they could be misleading due to the significant relative differences in regions with an OSI close to zero.

The combination of high OSI and low TAWSS correlates with an elevated risk of rupture and remodeling.[41,85] This gives rise to the HOLMES, a hemodynamic indicator defined according to Alimohammadi et al.,[85] that is,

$$\text{HOLMES} := \text{TAWSS}(1/2 - \text{OSI}), \tag{17}$$

to capture the intricacies of plaque formation and prediction. In Figure 13, we depict the HOLMES in the seventh cardiac cycle for the RWA, E90, and gHGO models. All models show high HOLMES values in the vicinity of the intimal tear and the proximal false lumen, while the distal false lumen features uniformly low HOLMES values. The HOLMES obtained via the RWA model depicts even higher values in the true lumen, signaling a more uniform and elevated TAWSS. Peaks in the entry tear region are most pronounced for the gHGO model, especially on the false lumen side (Figure 13(c)), demonstrating the interplay between geometrical features, tissue models, and resulting shear stress values. Overall, we observe similar patterns, although there are slight differences in the extreme values within the true lumen and in the size of the areas of increased HOLMES values.

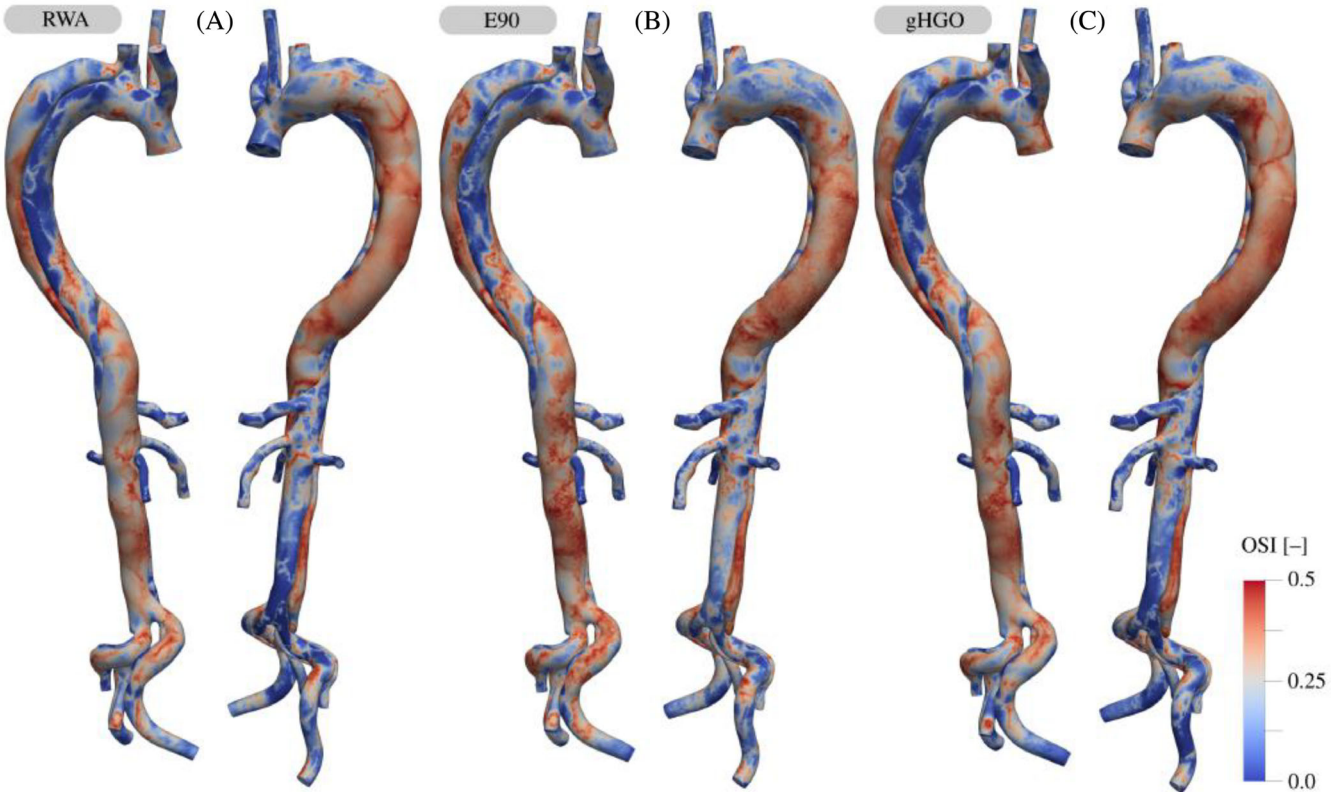

FIGURE 12 OSI integrated over the seventh cardiac cycle, determined using the RWA (A), E90 (B), and gHGO (C) models. Regions of high OSI indicate recirculatory flow and complex flow patterns present in both the true and especially the false lumen. There are differences between all three models, but the general patterns agree well. Note that the legend in (C) also applies to (A) and (B).

As a final hemodynamic indicator, we examine the endothelial cell activation potential (ECAP). Similar to HOLMES, it relates OSI and TAWSS via[87]

$$\mathrm{ECAP} := \frac{\mathrm{OSI}}{\mathrm{TAWSS}}. \tag{18}$$

This index is elevated in areas with high OSI and low TAWSS, indicating regions of endothelial vulnerability. Figure 14 shows ECAP computed over the seventh cardiac cycle for the RWA, E90, and gHGO models. The models considering vessel compliance show lower ECAP in the false lumen compared to RWA. All models predict low ECAP in the ascending aorta and arch, low to moderate values in the abdominal true lumen, and high ECAP in the false lumen. Differences between all models can be observed in the false lumen, where ECAP is high. The E90 and gHGO models display similar results, although with minor differences.

In summary, the differences in the hemodynamic indices TAWSS, OSI, HOLMES, and ECAP are significant in the visual comparison for the present case in the mentioned regions when comparing the RWA model, which neglects vessel compliance, with the E90 and gHGO models, which take tissue deformation into account. While the latter two FSI models generally produce similar results in terms of shear-stress-based indicators, the remaining small differences could still be relevant. We observed differences in TAWSS between the RWA and FSI simulations in the proximal true lumen, differences in OSI particularly in the false lumen in all three simulations presented, elevated HOLMES in the true lumen for RWA, increased peak HOLMES values for the gHGO models in the vicinity of the entry tear and an increase in ECAP as determined by the RWA simulation. In general, however, the spatial distributions and magnitudes are largely similar, with notable differences only in the areas mentioned above. The main objective of this study is to provide a detailed report on a single case study, and not to evaluate the statistical significance of these results. Based on these findings, it is not possible to draw broader conclusions for general cases.

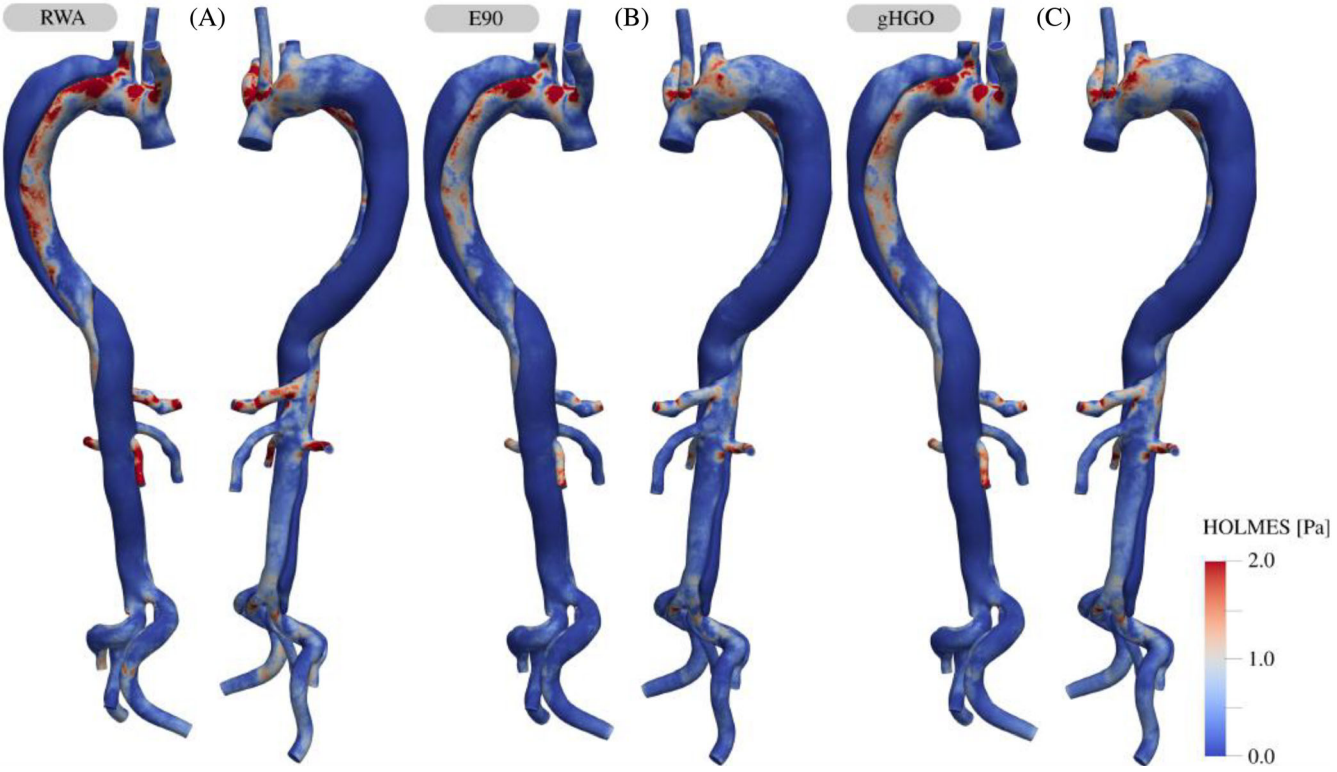

FIGURE 13 HOLMES integrated over the seventh cardiac cycle determined by the RWA (A), E90 (B), and gHGO (C) models. Areas of high HOLMES values indicate uni-directional high WSSs, while low HOLMES values are related to expansion and rupture of aortic tissue. Low HOLMES values are found in the false lumen in all three models, regions of high HOLMES are predominantly found in the true lumen where the simulation assuming rigid walls shows extended areas of high HOLMES values, and the gHGO model yields increased peak values in the vicinity of the entry tear (C). Note that the legend in (C) also applies to (A) and (B).

6.6 | Tissue stress measures

Exposing the tissue to high stresses and strains, potentially over a prolonged period, is associated with aortic remodeling, damage, or even rupture. However, computing the stress components in the material coordinate system that aligns with the circumferential, axial, and thickness directions of the vessel wall is cumbersome for three-dimensional bulk geometries reconstructed from clinical data and has rarely been reported in detail. To compute the stress magnitudes in these coordinate systems, the material orientation can be derived from structured meshing algorithms[88,89] or, as in the present case, as in Section 4.1. Due to the anisotropic microstructure and the associated direction-dependent material strength, measures such as the von Mises stress are not particularly suitable, since they do not take into account the local material orientation.

Figure 15 displays a simplified wall section with vectors indicating the directions: circumferential $\boldsymbol{E}_1$, axial $\boldsymbol{E}_2$, and normal $\boldsymbol{E}_3$. In the tangential plane spanned by $\boldsymbol{E}_1$ and $\boldsymbol{E}_2$, the mean fiber directions $\boldsymbol{M}_1$ and $\boldsymbol{M}_2$ are inclined by an in-plane angle $\pm\Phi$, while the out-of-plane angle is set to $\Theta = 0°$, which means that the mean fiber directions lie in the tangential plane. The Cauchy stress tensor $\boldsymbol{\sigma}_s$ of the solid can be written as

$$\boldsymbol{\sigma}_s = J^{-1}\boldsymbol{P}\boldsymbol{F}^{\mathrm{T}} = J^{-1}\boldsymbol{F}(\boldsymbol{S} + \boldsymbol{S}_0)\boldsymbol{F}^{\mathrm{T}}, \tag{19}$$

with the Jacobian $J := \det \boldsymbol{F}$, and the prestress tensor $\boldsymbol{S}_0$ according to Equation (9). The traction vector in the spatial configuration, denoted as $\boldsymbol{t} := \boldsymbol{\sigma}_s \boldsymbol{n}$, is decomposed into its tissue normal, circumferential and axial components. This decomposition uses the material orientation vectors mapped via the deformation gradient $\boldsymbol{F}$ as

$$\boldsymbol{e}_1 := \boldsymbol{F}\,\boldsymbol{E}_1, \quad \boldsymbol{e}_2 := \boldsymbol{F}\,\boldsymbol{E}_2.$$

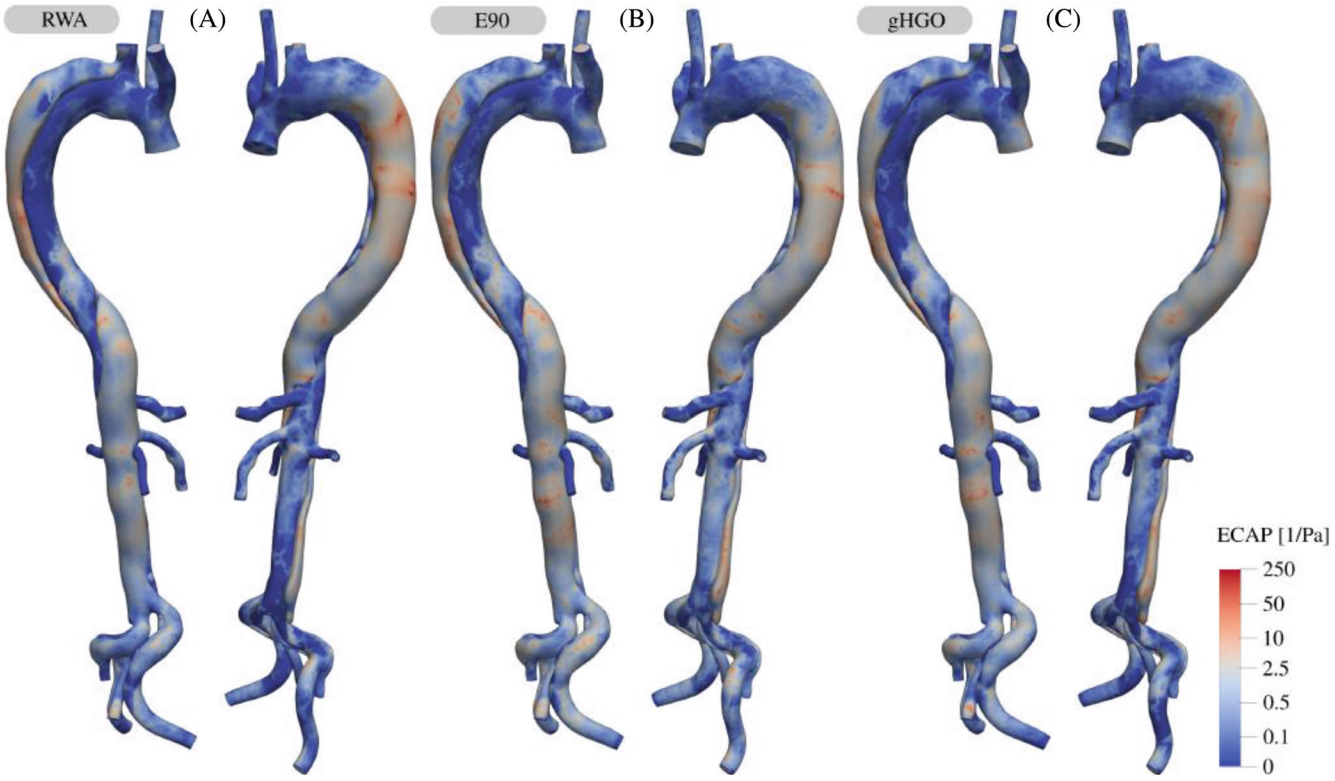

FIGURE 14 ECAP integrated over the seventh cardiac cycle obtained using the RWA (A), E90 (B), and gHGO (C) models. Regions of high ECAP indicate high OSI and low TAWSS and therefore endothelial vulnerability. ECAP is high in the false lumen for all models, whereas the results obtained with the RWA model show higher values. Note that the legend in (C) also applies to (A) and (B).

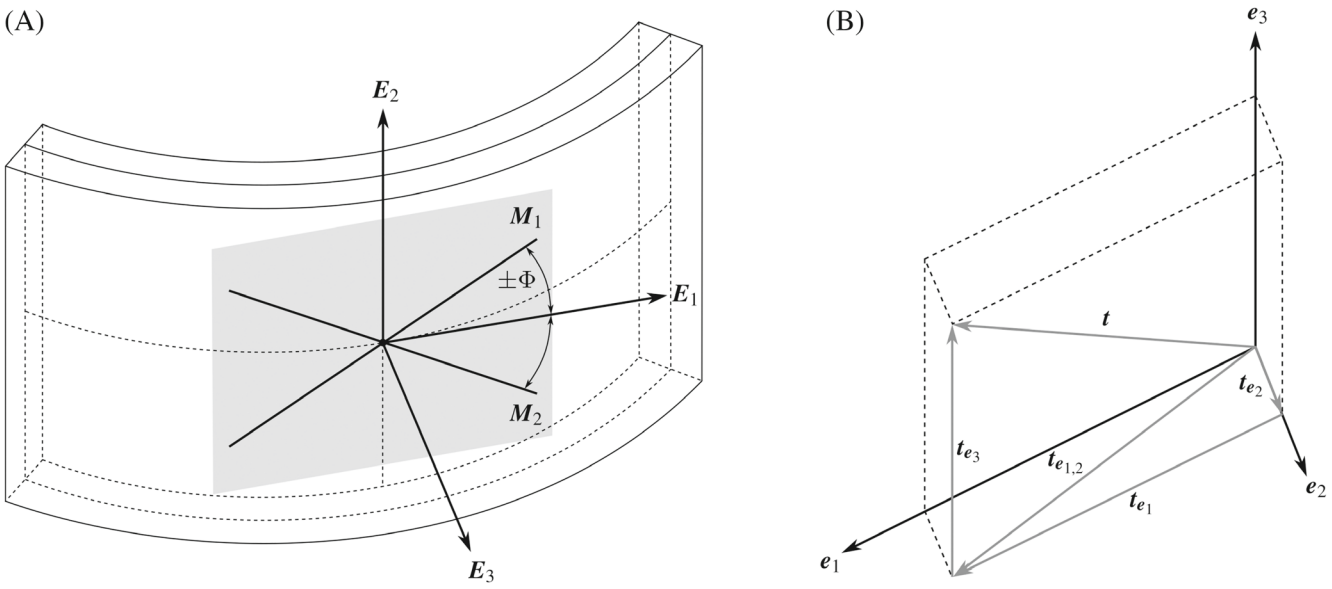

FIGURE 15 Material orientation in a simplified wall section (A), with vectors indicating the circumferential direction $\boldsymbol{E}_1$, the axial direction $\boldsymbol{E}_2$, and the tissue normal direction $\boldsymbol{E}_3$. (B) Decomposition of the traction vector in the transformed coordinate system spanned by $\boldsymbol{e}_1$, $\boldsymbol{e}_2$ and $\boldsymbol{e}_3$ into circumferential and axial shear components $\boldsymbol{t}_{e_1}$ and $\boldsymbol{t}_{e_2}$ and the tissue normal traction component $\boldsymbol{t}_{e_3}$.

The tissue normal direction $\boldsymbol{e}_3 := \boldsymbol{e}_1 \times \boldsymbol{e}_2$ leads to the normal traction vector $\boldsymbol{t}_{\boldsymbol{e}_3}$, that is,

$$\boldsymbol{t}_{\boldsymbol{e}_3} := \frac{\boldsymbol{t} \cdot \boldsymbol{e}_3}{||\boldsymbol{e}_3||^2}\, \boldsymbol{e}_3. \tag{20}$$

Additionally, there is a traction vector $\boldsymbol{t}_{\boldsymbol{e}_{1,2}} := \boldsymbol{t} - \boldsymbol{t}_{\boldsymbol{e}_3}$, which projects $\boldsymbol{t}$ onto the transformed tangential plane. The shear component vectors in the directions of $\boldsymbol{e}_1$ and $\boldsymbol{e}_2$ are given by

$$\boldsymbol{t}_{\boldsymbol{e}_1} := \frac{\boldsymbol{t}_{\boldsymbol{e}_{1,2}} \cdot \boldsymbol{e}_1}{||\boldsymbol{e}_1||^2}\, \boldsymbol{e}_1, \qquad \boldsymbol{t}_{\boldsymbol{e}_2} := \frac{\boldsymbol{t}_{\boldsymbol{e}_{1,2}} \cdot \boldsymbol{e}_2}{||\boldsymbol{e}_2||^2}\, \boldsymbol{e}_2, \tag{21}$$

all of which are shown in Figure 15 for a generic traction vector $\boldsymbol{t}$ and coordinate system spanned by $\boldsymbol{e}_1$, $\boldsymbol{e}_2$, and $\boldsymbol{e}_3$. In simple terms, these vectors can be viewed as reaction forces that act between the individual layers composing the vessel wall. In addition to these traction components, we also report the maximum positive principal stress, denoted as σ_I, which represents the largest positive eigenvalue of $\boldsymbol{\sigma}$.

The stress measures are evaluated at each finite element cell centroid, with the local material orientation given by the vector fields $\boldsymbol{E}_1$, $\boldsymbol{E}_2$, and $\boldsymbol{E}_3$. We compute every stress measure, that is, the maximum positive principal stress and the tissue normal and shear components, for selected time instants during the seventh cardiac cycle and separate them by tissue layer and model employed. The values for each quantity are sorted into 500 groups, each covering equal value ranges per dataset, effectively creating a histogram. Reporting on the group size and corresponding upper threshold allows for easier visualization. We can now examine the selected stress measures over time and compare the extreme values and their evolution over the cardiac cycle across tissue layers and models. In addition to the visual representation, we create box plots to quantify the observations. In these box plots, the time step featuring the highest values is further analyzed, considering the top 40 % highest values and removing the top 1 % data range, since we are interested in the maximum values without outliers. In each graph that displays data over time, the inflow profile scaling is indicated by a dashed black curve in the foreground to facilitate temporal correlation.

Figure 16 depicts the maximum positive principal stress σ_I in the adventia using models E90, NH, and gHGO. All plots have peak values during systole, where the largest deformations are observed. The E90 model shows a clear peak in the generated stresses, while the NH and gHGO models exhibit a smoother transition to the maximum value. The high Young's modulus selected for the E90 model, which is intended to achieve deformations in the range observed *in vivo*, leads to significantly higher peak values in the adventitia and media compared to the hyperelastic models. However, there are lower maximum positive principal stresses in the dissection flap.

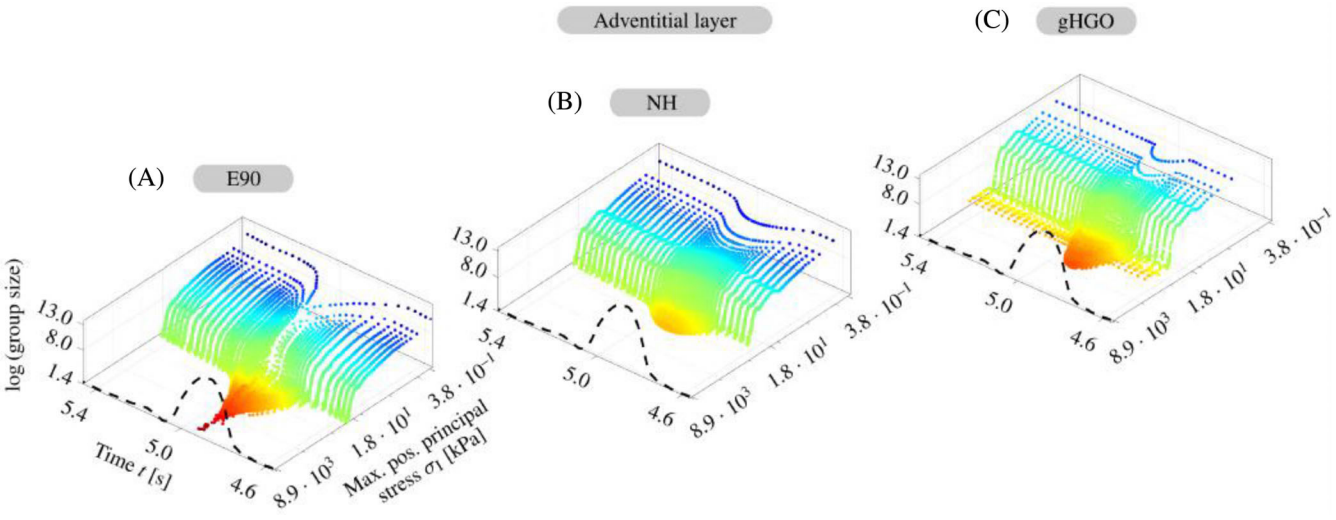

FIGURE 16 Maximum positive principal stresses in the adventitial layer sorted into 500 uniform groups covering the data range for the E90 (A), NH (B), and gHGO (C) models. Group size and corresponding upper thresholds over time and inflow scale (dashed curve in the foreground). The linear elastic model shows highest values and a clear peak, while the hyperelastic models show a more uniform development over time. Note that the axis labels in (A) also apply to (B) and (C).

Inspecting the box plots in Figure 17, we also note that the gHGO model has substantially increased values in the adventitia compared to the NH, gHGO90, and gHGO120 models. However, for the media and the dissection flap, the differences between the NH, gHGO, gHGO90, and gHGO120 models are less pronounced. The stiffness ratios between the tissue layers in each of the models result in different load distributions within the layers. Introducing fibers or increasing the shear modulus in the dissection flap obviously influences the observed stresses.

Regarding the traction component in the tissue normal direction, denoted as $\boldsymbol{t}_{\boldsymbol{e}_3}$, all models produce similar results in the group size/normal traction over time graphs, but differ in the maximum value observed. The systolic phase is again clearly visible in the results as, for example, shown for the dissection flap and E90, gHGO, and gHGO120 models in Figure 18. Compared to the maximum positive principal stress σ_{I} shown in Figure 16, we observe no decrease from the largest group size and lowest values to the smallest group size and largest values, but we do see a peak in the lower third to half of the value range. This peak in group size shifts to higher values during systole, but is rather similar across models and layers. If the gHGO model is used as the basis, the elimination of the fibers, as in the NH model, results in a redistribution of load, which subsequently leads to an increase in normal traction. Likewise, an increase in the shear

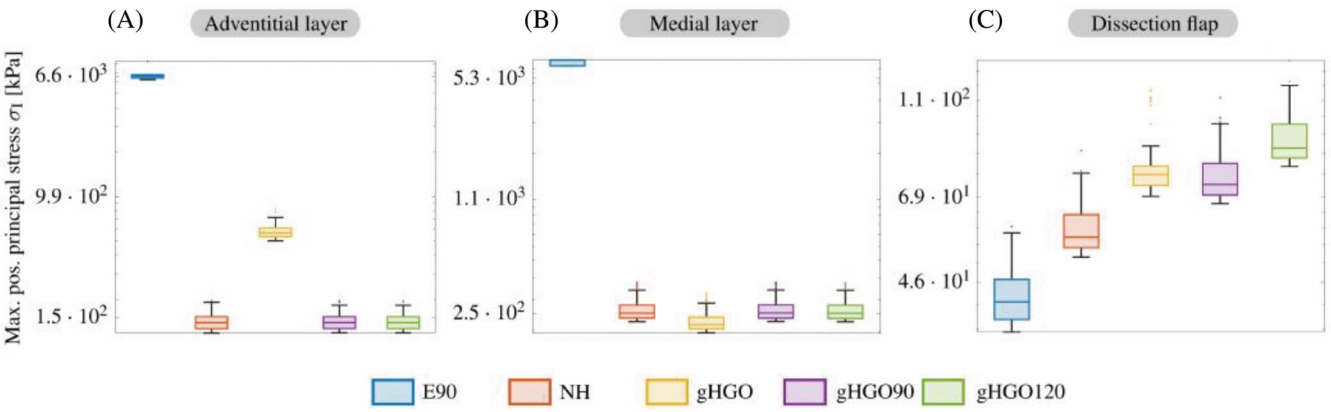

FIGURE 17 Box plots of the maximum positive principal stress at the time step with the highest value. The 40 % highest values are considered, with the top 1 % removed to omit outliers. The load distribution between the tissue layers (A to C) differs significantly when comparing the E90 with hyperelastic models. The gHGO model with base parameters also differs from the NH, gHGO90, and gHGO120 models in the adventitial layer, indicating different load-bearing behavior.

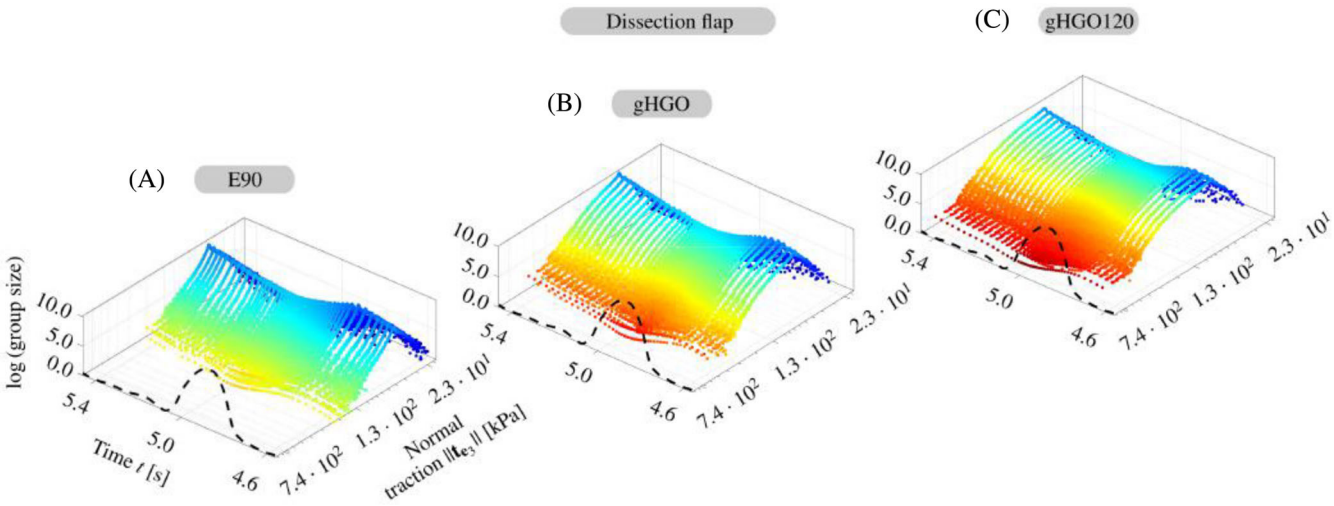

FIGURE 18 Normal traction component in the disscetion flap over time divided into 500 uniform groups covering the data range. Group size and corresponding upper thresholds over time, indicated by the inflow scale (dashed curve in the foreground). In the systolic phase the values are noticeably increased. An increase in the shear modulus in gHGO120 (C) compared to the base gHGO model (B) leads to increased normal traction, while the E90 model (A) yields lower values. Note that the axis labels in (A) also apply to (B) and (C).

modulus in the dissection flap, as in the gHGO90 and gHGO120 models, also leads to an increase of $\boldsymbol{t}_{\boldsymbol{e}_3}$, see Figure 19. Here, an increase in the dissection flap can be explained by its higher stiffness. The adventitia and media are also affected, which is due to a general shift in system behavior when a stiffer flap is used.

The traction components $\boldsymbol{t}_{\boldsymbol{e}_1}$ and $\boldsymbol{t}_{\boldsymbol{e}_2}$ display similar trends and temporal evolution in all models, so that we will therefore limit our discussion to the circumferential stress for brevity. Figure 20 shows the circumferential traction component in all tissue layers for the gHGO model. Above all, despite the increase in pressure, only very small variation can be observed over the cardiac cycle. For a comparison of the magnitudes of shear and normal components see Figures 19 and 21. One can immediately see that the in-plane traction components are significantly lower than the normal traction components. This suggests that the load-bearing behavior of the pressurized aortic tree is in the current model dominated by transmission through the wall directly into the viscoelastic support. In fact, this is very different from a pressurized pipe without external support, where circumferential stresses play a major role. Of course, this has a large impact on the stresses in the tissue, but further increasing the shear modulus of the tissue causes the parameters to quickly leave a realistic

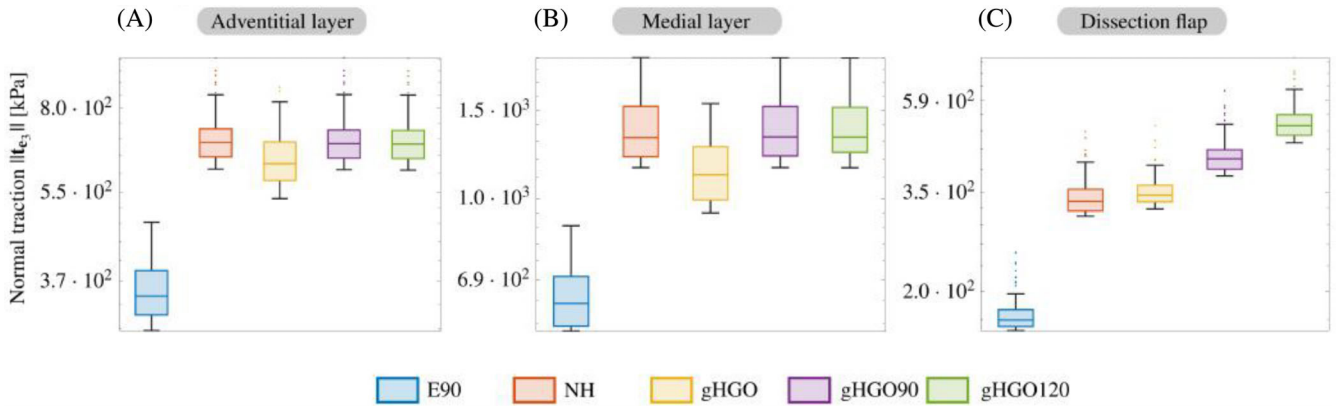

FIGURE 19 Box plots of tissue normal traction at the time step with the highest value. The 40 % highest values are considered, with the top 1 % removed to omit outliers. Increasing the shear modulus or neglecting the fiber contribution compared to the base gHGO model leads to an increase in normal traction in the hyperelastic models, while the E90 model leads to lower values in each layer.

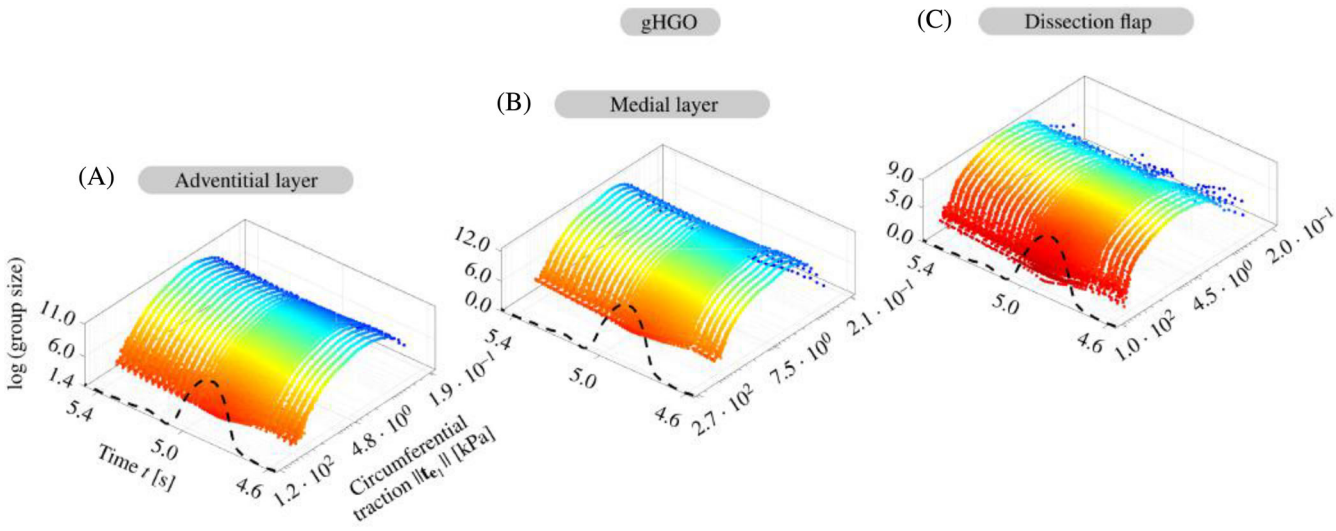

FIGURE 20 Circumferential traction component of the tissue layers (A to C) over time divided into 500 uniform groups covering the data range for the gHGO model. Group size and corresponding upper thresholds over time, indicated by the inflow scale (dashed curve in the foreground). In the systolic phase, the values are hardly increased and are generally well below the normal traction components, indicating direct load transfer to the viscoelastic support rather than an increase in diameter and resulting circumferential stresses. Note that the axis labels in (A) also apply to (B) and (C).

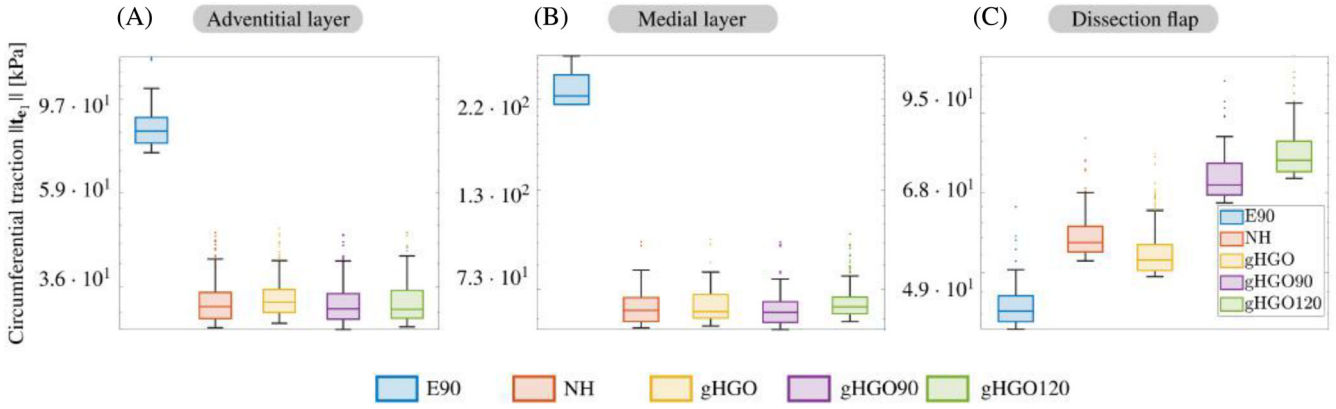

FIGURE 21 Box plots of circumferential traction in the time step with the highest value. The 40 % highest values are considered, with the top 1 % removed to omit outliers. The hyperelastic models produce significantly different results than the E90 model, while circumferential stresses are generally much lower than the normal traction component shown in Figure 19.

range. Increasing exponential contributions could alleviate some of these problems. However, larger strains and deformations are needed for noticeable differences, which is in contrast to the relatively small displacements typically observed *in vivo*. Thus, the tissue support parameters are maintained in a similar range to other works in the area,[15,60,61,90,91] again pointing to the need for improved models of viscoelastic support.

7 | DISCUSSION

The framework presented includes an anisotropic material model and takes the aortic wall into account in a layer-specific manner. It employs a non-Newtonian rheological model for blood flow, incorporates prestress and viscoelastic support of the aorta, and applies physiological boundary conditions for both blood and tissue. As a representative patient-specific application, a complex case of aortic dissection based on clinical data is considered. Different models with varying complexity are compared, taking as a baseline the combination of a nearly incompressible gHGO model with realistic fiber orientations and a Carreau fluid, both with realistic material parameters. The shear modulus in the dissection flap is artificially increased from $\mu_{s,1} = 62.1$ kPa by ≈50 % to $\mu_{s,1} = 90$ kPa, or by ≈100 % to $\mu_{s,1} = 120$ kPa, in the gHGO90 and gHGO120 models, respectively. Reducing the model complexity by omitting the fiber contributions yields a NH model. Assuming infinitesimal strains and applying Hooke's law, a linear elastic tissue model is created, which is combined with a Newtonian fluid in the E90 model. It is also possible that vessel compliance is completely neglected, leading to a pure flow problem on a fixed grid in the RWA model, which involves a Carreau fluid. Wherever possible, parameters optimized by Bäumler et al.[15] have been adopted to ensure better comparability and to reproduce flow splits and pressure levels, as discussed in Sections 2.2 and 4.4, while the additionally relevant tissue and blood parameters were taken from literature, see Sections 3.1 and 3.2. In the following, the current framework and the results obtained are placed in relation to other works in the field in order to highlight differences in the modeling and the results presented.

Dissection flap displacement. Using the gHGO model with physiological model parameters, we report a maximum dissection flap displacement of ≈3.5 mm in Figure 7, which underestimates the clinically measured maximum value of ≈8.7 mm. The previous study[15] on the same case found ≈1.4 mm up to ≈13.4 mm, depending on the material parameters selected for the tissue. Such values could not be achieved with the current approach. This limitation could be due to an overestimation of the stiffness of the dissection flap or to the geometric modeling of the transition from media to the dissection flap. Other works have reported values ≤1.5 mm[13,14,20] or up to 4.6 mm,[92] highlighting the patient specificity. The need for FSI methods therefore depends on the specific problem and must be carefully assessed in each individual case.

In a simple point-wise displacement norm (see Figure 7), differences between modeling approaches are easily observed, but complex nuances cannot be further assessed. Interestingly, the NH and gHGO models yield almost identical displacements, while E90, gHGO90, and gHGO120 lead to a reduced dissection flap displacement. Overall, the general shape of the displacement curve is similar for all models, while minor differences are only

observed in the diastolic phase. The exponential fiber contribution does not lead to notable differences in this blunt measure.

Volumetric flow rates. The flow split between the true and false lumina results in recirculatory flow in the proximal aorta. This also affects upstream regions and triggers vortices in the false lumen, leading to a reduction in WSS, which is associated with the loss of endothelial cells in the intimal layer.[93] Clinical studies suggest that low false lumen flow rates promote favorable clinical outcomes and reduce the likelihood of complications.[94,95]

The flow splits between the true and false lumina shown in Figure 8, computed over each of the models considering FSI with hyperelastic tissue models (NH, gHGO, gHGO90, and gHGO120), provide well-matching results. The increased stiffness introduced when considering fibers or increasing the dissection flap stiffness has little effect on the flow split due to the limited dissection flap displacements. Only the E90 model leads to notable differences in the distal regions and in the false lumen. This difference is due to the Newtonian fluid model and the dissection flap motion. When comparing these results with the RWA model, one can see the effects of vessel compliance and a mobile dissection flap on the true-to-false lumen flow split. This combination leads to a significantly reduced false lumen perfusion, which is in good agreement with the results presented by Bäumler et al.[15] For the current case, all hyperelastic models provide comparable results. However, the simplified models (E90 and RWA) give different results that affect the hemodynamic indicators, as explained below.

The differences between all in silico results and the MRI data are as pronounced as in Bäumler et al.[15] In that study and similarly herein, flow rates at the primary entry tear level are underestimated and retrograde flow in the distal false lumen was not observed. Due to the proximity of the primary entry tear to the aortic root, both the inlet profile and the Windkessel parameters for the supra-aortic vessels are critical factors in the true-to-false lumen flow split. However, as in many clinical scenarios, the former is not available, while the latter is fixed for better comparison with the work that presented results initially.[15] This leads to the conclusion that although the more complex models considered have a significant influence on the flow rates, the boundary conditions for the flow problem play an equally important role in modeling the present case. In terms of the clinical outcomes, underestimation of compliance leads to underestimation of false lumen flow, which in turn could underestimate the risk for late complications.[94,95]

True-to-false lumen pressure differences. The pressure difference between the true and the false lumen drives dissection flap motion. A more pronounced negative true-to-false lumen pressure difference – meaning higher pressure in the false lumen – is associated with the dilatation of the false lumen, true lumen collapse, and branch vessel occlusion.[96–99] A longitudinal study by Zhu et al.[11] identified a luminal pressure difference of more than 5 mmHg as a potential threshold value signaling unstable aortic growth.

The results presented in Figure 9 show small differences in the hyperelastic models, even with increased stiffness or by omitting the fiber contribution, while the E90 model differs slightly, but probably insignificantly from the rest of the FSI simulation results. Interestingly, ignoring vascular compliance, the RWA shows a pronounced negative peak in the abdominal aorta at systole and a reduced positive peak at early systole. In the current results we generally observe good agreement with the previous study.[15] However, there is less variability between our modeling choices, which is due to the reduced dissection flap motion resulting from the parameters chosen in the physiological range only. The influence of various tissue parameters is small given the hyperelastic models, while the RWA approach leads to an increase of up to ≈200 % in the negative peak value in early systole. Thus, using the threshold value of 5 mmHg, the RWA results indicate unstable aortic growth in the abdominal aorta, while the true-to-false lumen pressure difference determined via FSI results in a positive pressure difference during most of the cardiac cycle. Therefore, unlike the RWA prediction, the FSI prediction suggests favorable outcomes. The difference between the FSI and RWA models is potentially more drastic in the present case than in other configurations because the proximity of the primary entry tear to the aortic root and the resulting dissection flap displacements strongly influence the flow split between true and false lumina, hence the pressure difference.

Rheology. Non-Newtonian fluid models are known to significantly influence blood flow, especially in the presence of pathologies such as aortic dissections, stenoses, or aneurysms.[36–39] in silico studies adopting single- and multi-phase (non-)Newtonian models identified significant differences in shear-stress-based biomarkers,[14,41] which in turn are incorporated into thrombus formation models to predict long-term outcomes of aortic dissection.[83,100] In a simplified approach, we considered a single-phase generalized Newtonian fluid to capture the most relevant effects over a variable viscosity field. The present choice of parameters at the upper end of the physiological spectrum deliberately emphasizes the differences between Newtonian and generalized Newtonian models, as low average viscosity values are related to a smaller difference between upper and lower viscosity limits. Under these circumstances, for none of the non-Newtonian models

does the cross-sectional *average* viscosity reduce to the Newtonian limit, as illustrated in Figure 10. This suggests that low shear rates persist throughout the cardiac cycle in both the true and the false lumen. Due to the lower flow rate and larger cross-sectional area, the false lumen has lower shear rates and, therefore, higher viscosities, resulting in inhibited flow in the false lumen and faster diffusion of vortices and recirculations. We observe significant differences in the viscosity itself, and the potential influence of increased and varying viscosity on shear stress and related hemodynamic indicators is of direct clinical relevance.

Shear-stress-based indicators. TAWSSs and associated biomarkers are crucial for the interpretation and evaluation of vascular models. High TAWSS values correlate with an increased likelihood of rupture,[85,86] while low TAWSS values could increase the risk of endothelial cell degeneration and are often integrated in thrombus formation models.[83] High OSI values combined with low TAWSS are associated with an increased risk of rupture and remodeling.[41,85] By combining these two quantities, we obtain the HOLMES[85] and ECAP[87] hemodynamic indicators. These biomarkers indicate oscillatory shear of low magnitude, and thereby endothelial vulnerability. Consequently, these quantities allow assessing the risk associated with false lumen expansion, remodeling, and rupture.

Comparing TAWSS, OSI, HOLMES, and ECAP in Figures 11–14 for the RWA, E90, and gHGO models, it is observed that the RWA model produces both a lower TAWSS in the false lumen and a higher TAWSS in the true lumen and branching vessel regions. By completely ignoring vessel compliance and wall motion, we observe reduced shear stresses in the rigid false lumen. A rigid wall neglecting vessel expansion even under systolic flow conditions, results in a smaller hydraulic radius, leading to increased shear rates and consequently higher shear stresses in the true lumen. Consequently, the prediction of the RWA model appears more pessimistic. This trend extends to the OSI index and the derived HOLMES and ECAP biomarkers, where the RWA model indicates degraded conditions in both the true and false lumina. Depending on the threshold value employed, the RWA, E90, and hyperelastic models could lead to similar conclusions, but they can also suggest contradictory outcomes. However, accounting for model errors, the significance of these differences is beyond the scope of this study. The probability of rupture cannot be reliably derived from shear stress-based markers alone, as the load capacity of the tissue and resistance to rupture are completely ignored. High load, as predicted by HOLMES or ECAP is not the only influencing factor regarding failure. The same shear stress and related biomarkers (loading) could lead to different outcomes depending on local tissue strength (resistance). Here, local resistances must be taken into account.

Tissue stress measures. The present model considers a layer-by-layer representation of a patient-specific aorta, distinguishes between adventitia, media, and dissection flap, and accounts for the local fiber orientation. To fully exploit the model complexity when postprocessing the stresses, the anisotropic material properties were taken into account in tissue stress measures. Related works are based on the von Mises stress[20,21] or the maximum principal stress,[34,80] but none of these works relate the Cauchy stress directly to the microstructure orientation of the vessel. In this work, we investigated the spatio-temporal distribution of the latter stress measure, but also included the normal and tangential traction components of the tissue. The stress measures are calculated at selected time steps during the seventh cardiac cycle using the local coordinate system in each cell centroid. The resulting values are categorized into groups with equal data ranges to detail the sizes for each group. We found values of σ_{I} within the range reported in.[34,80] Differences between tissue layers and models are illustrated in Figure 17. The E90 model provided an order of magnitude higher values, but also provided displacements of the dissection flap displacement comparable to the hyperelastic models, see Figure 7. The hyperelastic models all gave similar maximum positive principal stresses. However, the values in the adventitia are higher when derived from the gHGO model. We hypothesize that the stiffness ratios between the different layers in each model influence the load distribution across the layers. Introducing fibers or increasing the shear modulus in the dissection flap influences the observed stresses. Using the current parameter set, all hyperelastic models produce mostly similar results. This suggests that existing methods that involve fairly stiff viscoelastic support may not reproduce the load-bearing behavior found *in vivo* sufficiently. If the viscoelastic support found *in vivo* is significantly lower than assumed in the literature, the relative importance of ring forces increases and thus the influence of constitutive modeling, anisotropy and fiber reinforcement.

Regarding the traction components in the normal direction of the tissue, the hyperelastic models have higher values than the linear E90 model, as shown in Figure 19. Among the hyperelastic models, the gHGO model resulted in the lowest normal traction in media and adventitia. An opposite trend can be observed for the circumferential traction components, see Figure 21. The linear elastic model E90 demonstrates increased shear, while the gHGO model has values that differ from other hyperelastic models in the dissection flap. Overall, the gHGO model results in a reduced shear-to-normal traction ratio. In all models, the pressure load is mainly transferred to the viscoelastic support, with less dependence on circumferential stresses. The interaction of tissue parameters and viscoelastic support thus shapes the stress state in the

tissue, which shifts from transduction in the normal direction of the tissue to a circumferential load distribution and the creation of ring forces. This highlights the need for careful design of the vessel's exterior support parameter fields.[90,91] Nevertheless, our findings support the use of hyperelastic solids with spatially varying parameters, as the results differ significantly from the E90 model, and differences can also be seen when comparing the anisotropic gHGO and isotropic NH models.

8 | LIMITATIONS

Patient-specific simulations of the cardiovascular system require a variety of assumptions to reach a complete problem description, that is, to define a complete initial boundary-value problem. As model complexity increases, the number of model parameters and the associated tuning possibilities increase. In this present study, we focused on a comparison of fluid and solid modeling assumptions that form the basis of the computational framework. We compare these modeling assumptions by quantifying their outcomes using hemodynamic indicators and tissue stress measures, which are strongly influenced by parameter selection. Therefore, the selected parameters for each of the fluid and tissue models limit the generality of the conclusions drawn. Extrapolation of the presented results to other cases of aortic dissection is cumbersome. However, the single case analyzed here can be viewed as a typical example and the conclusions can therefore be transferred to similar cases. Although the tissue layer thickness and parameters are assumed to be constant for each tissue layer, it is important to note that this approach goes beyond the state-of-the-art in modeling aortic dissection. With such intricate geometries, the layer-specific subdivision of the aortic wall represents a particular challenge. In order to avoid shell elements, the intimal layer is merged with the media. The outcomes of the nonlinear coupled system are also influenced by other factors such as the Windkessel parameters and inflow profile, which are kept constant for all models considered, although tailored parameter sets may fit the clinical data better than the considered set. The framework would therefore greatly benefit from automated parameter fitting to better match the clinical data for each of the models considered.

9 | CONCLUDING REMARKS

We introduced a robust and comprehensive numerical framework tailored to the simulation of vascular flow and tissue deformation with a focus on aortic dissection. Although it combines a number of existing techniques, the particular contribution of this work lies in the representation of the vessel wall layers – adventitia, media, and dissection flap – each of which is endowed with specific parameters. Automated construction of physiological material coordinate systems to correctly align the microstructure is key to applying anisotropic hyperelastic models in patient-specific cases where the dissection flap present in aortic dissection cases requires nonstandard treatment. The different variants of the models considered involve rigid wall flow problems and FSI simulations that couple Newtonian and non-Newtonian fluids with linear elastic, nearly incompressible (an-)isotropic hyperelastic, possibly fiber-reinforced continua and adopting layer-specific parameters. The results are carefully analyzed using established hemodynamic indicators and other biomarkers. We evaluated and compared dissection flap displacements, flow rates in both true and false lumina, true-to-false lumen pressure differences, and shear stress-based indicators such as TAWSS, OSI, HOLMES, and ECAP. The results presented agree well with the previous study by Bäumler et al.,[15] but extend the results toward more complex constitutive behavior and a deeper analysis using hemodynamic indicators and tissue stress measures.

This study provides detailed results incorporating the microstructure of the aortic wall and the stress measures used, shedding insights into *in vivo* stress conditions within a patient-specific geometry under physiological conditions. Most of the results presented show significant differences between rigid wall flow simulations and the linear elastic and hyperelastic models in an FSI approach. However, some hemodynamic indicators show only small variations. The detailed analysis of the normal and shear stress components of the tissue showed that a significant portion of the pressure load is transferred to the viscoelastic support, while the contribution of circumferential tractions depends on the tissue-to-support stiffness ratio. This latter conclusion has received little attention in the past and motivates future investigations into parameter identification in patient-specific scenarios of vascular flow.

In summary, the aim of the computational study has been to evaluate the increased numerical effort required for FSI modeling. Expectations suggest factors of 5 to 20, not including the time spent on mesh construction and further preprocessing. Based on the current case, one could argue that certain hemodynamic indicators only require

rigid wall simulations instead of comprehensive FSI simulations, while others showed greater differences. One could also consider conducting a detailed stress analysis in the tissue using only systolic flow conditions, which might provide somewhat similar results to FSI but at considerably reduced costs. However, it is important to highlight that the uncertainty associated with patient-specific modeling and associated parameters limits the significance of individual models of the vascular system, including the present one, again highlighting the need for further research in this area.

ACKNOWLEDGMENTS

The authors acknowledge the support of Graz University of Technology, Austria, through the LEAD Project (2018–2024) "Mechanics, Modeling, and Simulation of Aortic Dissection" to MRP; and the Bavarian State Ministry of Science and the Arts for funding the Augsburg AI Production Network as part of the High-Tech Agenda Plus to RS. Open Access funding enabled and organized by Projekt DEAL.

CONFLICT OF INTEREST STATEMENT

The authors declare that the research was conducted in the absence of any commercial or financial relationships that could be construed as a potential conflict of interest.

DATA AVAILABILITY STATEMENT

The dataset for this study can be found online in the Vascular Model Repository available at https://www.vascularmodel.com/ (model '0160_H_AO_AOD').

ORCID

Richard Schussnig https://orcid.org/0000-0002-0541-2544
Malte Rolf-Pissarczyk https://orcid.org/0000-0003-4467-5483
Kathrin Bäumler https://orcid.org/0000-0002-2126-5919
Thomas-Peter Fries https://orcid.org/0000-0003-1210-1557
Gerhard A. Holzapfel https://orcid.org/0000-0001-8119-5775
Martin Kronbichler https://orcid.org/0000-0001-8406-835X

REFERENCES

1. Abazari MA, Rafieianzab D, Soltani M, Alimohammadi M. The effect of beta-blockers on hemodynamic parameters in patient-specific blood flow simulations of type-B aortic dissection: a virtual study. *Sci Rep*. 2021;11:16058.
2. Xu H, Zhenfeng L, Huiwu D, et al. Hemodynamic parameters that may predict false-lumen growth in type-B aortic dissection after endovascular repair: a preliminary study on long-term multiple follow-ups. *Med Eng Phys*. 2017;50:12-21.
3. Armour CH, Guo B, Saitta S, et al. Evaluation and verification of patient-specific modelling of type B aortic dissection. *Comput Biol Med*. 2022;140:105053.
4. Moretti S, Tauro F, Orrico M, Mangialardi N, Facci AL. Comparative analysis of patient-specific aortic dissections through computational fluid dynamics suggests increased likelihood of degeneration in partially thrombosed false lumen. *Bioengineering*. 2023;10:316.
5. Kimura N, Nakamura M, Takagi R, et al. False lumen/true lumen wall pressure ratio is increased in acute non-A non-B aortic dissection. *Interact Cardiovasc Thorac Surg*. 2022;3(3):ivac138.
6. Wan Ab Naim WN, Ganesan P, Sun Z, Osman K, Einly L. The impact of the number of tears in patient-specific Stanford type B aortic dissection aneurysm: CFD simulation. *J Mech Med Biol*. 2014;14(2):20.
7. Dillon-Murphy D, Noorani A, Nordsletten D, Figueroa CA. Multi-modality image-based computational analysis of haemodynamics in aortic dissection. *Biomech Model Mechanobiol*. 2016;15:857-876.
8. Yu S, Liu W, Wong RH, Underwood M, Wang D. The potential of computational fluid dynamics simulation on serial monitoring of hemodynamic change in type B aortic dissection. *Cardiovasc Intervent Radiol*. 2016;39(8):1090-1098.
9. Xiong Z, Yang P, Li D, Qiu Y, Zheng T, Hu J. A computational fluid dynamics analysis of a patient with acute non-A-non-B aortic dissection after type I hybrid arch repair. *Med Eng Phys*. 2020;77:43-52.
10. Li Z, Xu H, Armour CH, et al. The necessity to seal the re-entry tears of aortic dissection after TEVAR: a hemodynamic indicator. *Front Bioeng Biotechnol*. 2022;10:831903.
11. Zhu Y, Xu XY, Rosendahl U, Pepper J, Mirsadraee S. Prediction of aortic dilatation in surgically repaired type A dissection: a longitudinal study using computational fluid dynamics. *JTCVS Open*. 2022;9:11-27.
12. Parker LP, Reutersberg B, Syed MBJ, et al. Proximal false lumen thrombosis is associated with low false lumen pressure and fewer complications in type B aortic dissection. *J Vasc Surg*. 2022;75(4):1181-1190.

13. Alimohammadi M, Sherwood J, Karimpour M, Agu O, Balabani S, Díaz-Zuccarini V. Aortic dissection simulation models for clinical support: fluid–structure interaction vs. rigid wall models. *Biomed Eng Online*. 2015;14:34.
14. Qiao Y, Zeng Y, Ding Y, Fan J, Luo K, Zhu T. Numerical simulation of two-phase non-Newtonian blood flow with fluid–structure interaction in aortic dissection. *Comput Methods Biomech Biomed Engin*. 2019;22(6):620-630.
15. Bäumler K, Vedula V, Sailer AM, et al. Fluid–structure interaction simulations of patient-specific aortic dissection. *Biomech Model Mechanobiol*. 2020;19:1607-1628.
16. Khannous F, Guivier-Curien C, Gaudry M, Piquet P, Deplano V. Residual type B aortic dissection FSI modeling. *Comput Methods Biomech Biomed Engin*. 2020;23(sup1):S153-S155.
17. Bonfanti M, Balabani S, Alimohammadi M, Agu O, Homer-Vanniasinkam S, Díaz-Zuccarini V. A simplified method to account for wall motion in patient-specific blood flow simulations of aortic dissection: comparison with fluid–structure interaction. *Med Eng Phys*. 2018;58:72-79.
18. Bonfanti M, Balabani S, Greenwood JP, Puppala S, Homer-Vanniasinkam S, Díaz-Zuccarini V. Computational tools for clinical support: a multi-scale compliant model for haemodynamic simulations in an aortic dissection based on multi-modal imaging data. *J R Soc Interface*. 2017;14(136):20170632.
19. Zimmermann J, Bäumler K, Loecher M, et al. Hemodynamic effects of tear size in aortic dissections: comparing in vitro flow magnetic resonance imaging with fluid-structure interaction simulations. *Sci Rep*. 2023;13(1):22557.
20. Zhu Y, Mirsadraee S, Rosendahl U, Pepper J, Xu XY. Fluid–structure interaction simulations of repaired type A aortic dissection: a comprehensive comparison with rigid wall models. *Front Physiol*. 2022;13:913457.
21. Wang X, Ghayesh MH, Kotousov A, Zander AC, Dawson JA, Psaltis PJ. Fluid–structure interaction study for biomechanics and risk factors in Stanford type A aortic dissection. *Int J Numer Method Biomed Eng*. 2023;39:e3736.
22. Updegrove A, Wilson NM, Merkow J, Lan H, Marsden AL, Shadden SC. SimVascular: an open source pipeline for cardiovascular simulation. *Ann Biomed Eng*. 2016;45:525-541.
23. Schmidt R, Singh K. Meshmixer: an interface for rapid mesh composition. *ACM SIGGRAPH 2010 Talks, SIGGRAPH'10*. ACM; 2010:1.
24. Geuzaine C, Remacle JF. Gmsh: a 3-D finite element mesh generator with built-in pre- and post-processing facilities. *Int J Numer Methods Eng*. 2009;79(11):1309-1331.
25. Holzapfel GA, Niestrawska JA, Ogden RW, Reinisch AR, Schriefl AJ. Modelling non-symmetric collagen fibre dispersion in arterial walls. *J R Soc Interface*. 2015;12(106):1-14.
26. Holzapfel GA. *Nonlinear Solid Mechanics. A Continuum Approach for Engineering*. John Wiley & Sons; 2000.
27. Gasser TC, Ogden RW, Holzapfel GA. Hyperelastic modelling of arterial layers with distributed collagen fibre orientations. *J R Soc Interface*. 2006;3(6):15-35.
28. Holzapfel GA, Ogden RW. On the tension–compression switch in soft fibrous solids. *Eur J Mech A Solids*. 2015;49:561-569.
29. Bonet J, Wood RD. *Nonlinear Continuum Mechanics for Finite Element Analysis*. 2nd ed. Cambridge University Press; 2008.
30. Chung J, Hulbert GM. A time integration algorithm for structural dynamics with improved numerical dissipation: the generalized-α method. *J Appl Mech Trans ASME*. 1993;60(2):371-375.
31. Schussnig R, Pacheco DRQ, Kaltenbacher M, Fries TP. Semi-implicit fluid–structure interaction in biomedical applications. *Comput Methods Appl Mech Eng*. 2022;400:115489.
32. Schussnig R. *Generalised Newtonian Fluids in Cardiovascular Fluid–Structure Interaction*. PhD thesis. Monographic Series TU Graz in Structural Analysis. Graz; 2023.
33. Weisbecker H, Pierce DM, Regitnig P, Holzapfel GA. Layer-specific damage experiments and modeling of human thoracic and abdominal aortas with non-atherosclerotic intimal thickening. *J Mech Behav Biomed Mater*. 2012;12:93-106.
34. Rolf-Pissarczyk M, Wollner MP, Pacheco DRQ, Holzapfel GA. Efficient computational modelling of smooth muscle orientation and function in the aorta. *Proc R Soc A*. 2021;477:20210592.
35. Fleischmann D, Afifi RO, Casanegra AI, et al. Imaging and surveillance of chronic aortic dissection: a scientific statement from the American Heart Association. *Circ Cardiovasc Imaging*. 2022;15(3):e000075.
36. Galdi GP, Robertson AM, Rannacher R, Turek S. *Hemodynamical Flows. 37 of Oberwolfach Seminars*. Birkhäuser; 2008.
37. Bernsdorf J, Wang D. Non-Newtonian blood flow simulation in cerebral aneurysms. *Comput Math Appl*. 2009;58(5): 1024-1029.
38. John L, Pustějovská P, Steinbach O. On the influence of the wall shear stress vector form on hemodynamic indicators. *Comput Vis Sci*. 2017;18(4-5):113-122.
39. Ranftl S, Müller TS, Windberger U, von der Linden W, Brenn G. A Bayesian approach to blood rheological uncertainties in aortic hemodynamics. *Int J Numer Method Biomed Eng*. 2023;39(4):e3576.
40. Abbasian M, Shams M, Valizadeh Z, Moshfegh A, Javadzadegan A, Cheng S. Effects of different non-Newtonian models on unsteady blood flow hemodynamics in patient-specific arterial models with in-vivo validation. *Comput Methods Prog Biomed*. 2020;186: 105185.
41. Qiao Y, Fan J, Ding Y, Luo PK, Zhu T. A primary computational fluid dynamics study of pre- and post-TEVAR with intentional left subclavian artery coverage in a type B aortic dissection. *J Biomech Eng*. 2019;141(11):111002.
42. Fatma K, Carine GC, Marine G, Philippe P, Deplano V. Numerical modeling of residual type B aortic dissection: longitudinal analysis of favorable and unfavorable evolution. *Med Biol Eng Comput*. 2022;60:769-783.

43. Hirt CW, Amsden AA, Cook JL. An arbitrary Lagrangian-Eulerian computing method for all flow speeds. *J Comput Phys*. 1974;14(3):227-253.
44. Hughes TJR, Liu WK, Zimmermann TK. Lagrangian-Eulerian finite element formulation for incompressible viscous flows. *Comput Methods Appl Mech Eng*. 1981;29(3):329-349.
45. Donea J, Huerta A, Ponthot JP, Rodríguez-Ferran A. Arbitrary Lagrangian-Eulerian Methods. *Encyclopedia of Computational Mechanics*. 2nd ed. John Wiley & Sons; 2017:1-23.
46. Pacheco DRQ, Schussnig R, Fries TP. An efficient split-step framework for non-Newtonian incompressible flow problems with consistent pressure boundary conditions. *Comput Methods Appl Mech Eng*. 2021;382:113888.
47. Brooks AN, Hughes TJR. Streamline upwind/Petrov-Galerkin formulations for convection dominated flows with particular emphasis on the incompressible Navier-Stokes equations. *Comput Methods Appl Mech Eng*. 1982;32(1):199-259.
48. Bayer JD, Blake RC, Plank G, Trayanova NA. A novel rule-based algorithm for assigning myocardial fiber orientation to computational heart models. *Ann Biomed Eng*. 2012;40(10):2243-2254.
49. Marx L, Niestrawska JA, Gsell MAF, Caforio F, Plank G, Augustin CM. Robust and efficient fixed-point algorithm for the inverse elastostatic problem to identify myocardial passive material parameters and the unloaded reference configuration. *J Comput Phys*. 2022;463:111266.
50. Schussnig R, Rolf-Pissarczyk M, Holzapfel GA, Fries TP. Fluid–structure interaction simulations of aortic dissection. *Proc Appl Math Mech*. 2021;20(1):e202000125.
51. Gee MW, Reeps C, Eckstein HH, Wall WA. Prestressing in finite deformation abdominal aortic aneurysm simulation. *J Biomech*. 2009;42(11):1732-1739.
52. Gee MW, Förster C, Wall WA. A computational strategy for prestressing patient-specific biomechanical problems under finite deformation. *Int J Numer Methods Biomed Eng*. 2010;26(1):52-72.
53. Hsu MC, Bazilevs Y. Blood vessel tissue prestress modeling for vascular fluid–structure interaction simulation. *Finite Elem Anal Des*. 2011;47(6):593-599.
54. Baek H, Karniadakis GE. A convergence study of a new partitioned fluid–structure interaction algorithm based on fictitious mass and damping. *J Comput Phys*. 2012;231(2):629-652.
55. Bukač M, Čanić S, Glowinski R, Tambača J, Quaini A. Fluid–structure interaction in blood flow capturing non-zero longitudinal structure displacement. *J Comput Phys*. 2013;235:515-541.
56. Wick T. Flapping and contact FSI computations with the fluid-solid interface-tracking/interface-capturing technique and mesh adaptivity. *Comput Mech*. 2014;53(1):29-43.
57. Richter T. *Fluid-Structure Interactions: Models, Analysis and Finite Elements*. Springer International Publishing; 2017.
58. Radtke L, Larena-Avellaneda A, Debus ES, Düster A. Convergence acceleration for partitioned simulations of the fluid-structure interaction in arteries. *Comput Mech*. 2016;57:901-920.
59. de Villiers AM, McBride AT, Reddy BD, Franz T, Spottiswoode BS. A validated patient-specific FSI model for vascular access in haemodialysis. *Biomech Model Mechanobiol*. 2018;17(2):479-497.
60. Moireau P, Xiao N, Astorino M, et al. External tissue support and fluid-structure simulation in blood flows. *Biomech Model Mechanobiol*. 2012;11(1-2):1-18.
61. Reymond P, Crosetto P, Deparis S, Quarteroni A, Stergiopulos N. Physiological simulation of blood flow in the aorta: comparison of hemodynamic indices as predicted by 3-D FSI, 3-D rigid wall and 1-D models. *Med Eng Phys*. 2013;35(6):784-791.
62. Jin S, Oshinski J, Giddens DP. Effects of wall motion and compliance on flow patterns in the ascending aorta. *J Biomech Eng*. 2003;125(3):347-354.
63. Beller CJ, Labrosse MR, Thubrikar MJ, Robicsek F. Role of aortic root motion in the pathogenesis of aortic dissection. *Circulation*. 2004;109:763-769.
64. Beller CJ, Labrosse MR, Thubrikar MJ, Robicsek F. Finite element modeling of the thoracic aorta: including aortic root motion to evaluate the risk of aortic dissection. *J Med Eng Technol*. 2008;32(2):167-170.
65. Singh SD, Xu XY, Pepper JR, Izgi C, Treasure T, Mohiaddin RH. Effects of aortic root motion on wall stress in the Marfan aorta before and after personalised aortic root support (PEARS) surgery. *J Biomech*. 2016;49(10):2076-2084.
66. Plonek T, Zak M, Burzynska K, et al. The combined impact of mechanical factors on the wall stress of the human ascending aorta – a finite elements study. *BMC Cardiovasc Disord*. 2017;17(1):297.
67. Plonek T, Zak M, Rylski B, et al. Wall stress correlates with intimal entry tear localization in type A aortic dissection. *Interact Cardiovasc Thorac Surg*. 2018;27(6):797-801.
68. Subramaniam DR, Gutmark E, Andersen N, et al. Influence of material model and aortic root motion in finite element analysis of two exemplary cases of proximal aortic dissection. *J Biomech Eng*. 2021;143(1):014504.
69. Wei W, Evin M, Rapacchi S, et al. Investigating heartbeat-related in-plane motion and stress levels induced at the aortic root. *Biomed Eng Online*. 2019;19(18):1-15.
70. Kim T, Tjahjadi NS, He X, et al. Three-Dimensional characterization of aortic root motion by vascular deformation mapping. *J Clin Med*. 2023;12(13):4471.
71. Kozerke S, Scheidegger MB, Pedersen EM, Boesiger P. Heart motion adapted cine phase-contrast flow measurements through the aortic valve. *Magn Reson Med*. 1999;42(5):970-978.
72. Stuber M, Scheidegger MB, Fischer SE, et al. Alterations in the local myocardial motion pattern in patients suffering from pressure overload due to aortic stenosis. *Circulation*. 1999;100(4):361-368.

73. Takizawa K, Christopher J, Tezduyar TE, Sathe S. Space-time finite element computation of arterial fluid-structure interactions with patient-specific data. *Int J Numer Methods Biomed Eng*. 2010;26(1):101-116.
74. Laskey WK, Parker HG, Ferrari VA, Kussmaul WG, Noordergraaf A. Estimation of total systemic arterial compliance in humans. *J Appl Physiol*. 1990;69(1):112-119.
75. Kim HJ, Vignon-Clementel IE, Figueroa CA, Jansen KE, Taylor CA. Developing computational methods for three-dimensional finite element simulations of coronary blood flow. *Finite Elem Anal Des*. 2010;46(6):514-525.
76. Arndt D, Bangerth W, Feder M, et al. The deal.II Library, Version 9.4. *J Numer Math*. 2022;30(3):231-246.
77. Heroux MA, Willenbring JM. A new overview of the Trilinos project. *Sci Program*. 2012;20(2):83-88.
78. Degroote J, Bathe KJ, Vierendeels J. Performance of a new partitioned procedure versus a monolithic procedure in fluid–structure interaction. *Comput Struct*. 2009;87(11-12):793-801.
79. Chen D, Müller-Eschner M, Tengg-Kobligk vH, et al. A patient-specific study of type-B aortic dissection: evaluation of true-false lumen blood exchange. *Biomed Eng Online*. 2013;12(65):1-16.
80. Rolf-Pissarczyk M, Li K, Fleischmann D, Holzapfel GA. A discrete approach for modeling degraded elastic fibers in aortic dissection. *Comput Methods Appl Mech Eng*. 2021;373:113511.
81. Menichini C, Cheng Z, Gibbs R, Xu XY. A computational model for false lumen thrombosis in type B aortic dissection following thoracic endovascular repair. *J Biomech*. 2017;66:36-43.
82. Chong M, Gu B, Armour C. An integrated fluid–structure interaction and thrombosis model for type B aortic dissection. *Biomech Model Mechanobiol*. 2022;21:261-275.
83. Jafarinia A, Armour CG, Gibbs RGJ, Xu XY, Hochrainer T. Shear-driven modelling of thrombus formation in type B aortic dissection. *Front Bioeng Biotechnol*. 2022;10:831903.
84. Schussnig R, Dreymann S, Jafarinia A, Hochrainer T, Fries TP. A semi-implicit method for thrombus formation in haemodynamic fluid–structure interaction. *Proceedings of the 8th European Congress on Computational Methods in Applied Sciences and Engineering*. ECCOMAS; 2022:1-12.
85. Alimohammadi M, Pichardo-Almarza C, Agu O, Díaz-Zuccarini V. Development of a patient-specific multi-scale model to understand atherosclerosis and calcification locations: comparison with in vivo data in an aortic dissection. *Front Physiol*. 2016;7:1-15.
86. Alimohammadi M. *Aortic Dissection: Simulation Tools for Disease Management and Understanding*. Springer International Publishing; 2018.
87. Di Achille P, Tellides G, Figueroa CA, Humphrey JD. A haemodynamic predictor of intraluminal thrombus formation in abdominal aortic aneurysms. *Proc R Soc A*. 2014;470:1-22.
88. Bošnjak D, Pepe A, Schussnig R, Schmalstieg D, Fries TP. Higher-order block-structured hex meshing of tubular structures. *Eng Comput*. 2023;05:1-21.
89. Bošnjak D, Fries TP. Block-structured mesh generation from implicit geometries for cardiovascular applications. *PAMM*. 2023;23:e202300023.
90. Moireau P, Bertoglio C, Xiao N, et al. Sequential identification of boundary support parameters in a fluid–structure vascular model using patient image data. *Biomech Model Mechanobiol*. 2013;12(3):475-496.
91. Shidhore TC, Cebull HL, Madden MC, Christov IC, Rayz VL, Goergen CJ. Estimating external tissue support parameters with fluid–structure interaction models from 4D ultrasound of murine thoracic aortae. *Eng Comput*. 2022;38(5):4005-4022.
92. Chong MY, Gu B, Chan BT, Ong ZC, Xu XY, Lim E. Effect of intimal flap motion on flow in acute type B aortic dissection by using fluid-structure interaction. *Int J Numer Methods Biomed Eng*. 2020;36(12):e3399.
93. Aparício P, Mandaltsi A, Boamah J, et al. Modelling the influence of endothelial heterogeneity on the progression of arterial disease: application to abdominal aortic aneurysm evolution. *Int J Numer Methods Biomed Eng*. 2014;30(5):563-586.
94. Song SW, Chang BC, Cho BK, et al. Effects of partial thrombosis on distal aorta after repair of acute DeBakey type I aortic dissection. *J Thorac Cardiovasc Surg*. 2010;139(4):841-847.e1.
95. Halstead JC, Meier M, Etz C, et al. The fate of the distal aorta after repair of acute type A aortic dissection. *J Thorac Cardiovasc Surg*. 2007;133(1):127-135.e1.
96. Chung J, Elkins C, Sakai T, et al. True-lumen collapse in aortic dissection: part I. Evaluation of causative factors in phantoms with pulsatile flow. *Radiology*. 2000;214(1):87-98.
97. Tsai TT, Evangelista A, Nienaber CA, et al. Partial thrombosis of the false lumen in patients with acute type B aortic dissection. *N Engl J Med*. 2007;357(4):349-359.
98. Karmonik C, Bismuth J, Shah DJ, Davies MG, Purdy D, Lumsden AB. Computational study of haemodynamic effects of entry- and exit-tear coverage in a DeBakey type III aortic dissection: technical report. *Eur J Vasc Endovasc Surg*. 2011;42(2):172-177.
99. Berguer R, Parodi JC, Schlicht M, Khanafer K. Experimental and clinical evidence supporting septectomy in the primary treatment of acute type B thoracic aortic dissection. *Ann Vasc Surg*. 2015;29(2):167-173.
100. Jafarinia A, Melito GM, Müller TS, et al. Morphological parameters affecting false lumen thrombosis following type B aortic dissection: a systematic study based on simulations of idealized models. *Biomech Model Mechanobiol*. 2023;22:885-904.
101. Schriefl AJ, Zeindlinger G, Pierce D, Regitnig P, Holzapfel GA. Determination of the layer-specific distributed collagen fibre orientations in human thoracic and abdominal aortas and common iliac arteries. *J R Soc Interface*. 2012;9(71):1275-1286.
102. Wollner MP. *Semi-analytical Investigation of the Transmural Alignment of Vascular Smooth Muscle Cells*. diplomarbeit. Technische Universität Dresden; 2020.

103. Gültekin O, Dal H, Holzapfel GA. On the quasi-incompressible finite element analysis of anisotropic hyperelastic materials. *Comput Mech*. 2019;63:443-453.
104. Simo JC, Miehe C. Associative coupled thermoplasticity at finite strains: Formulation, numerical analysis and implementation. *Comput Methods Appl Mech Eng*. 1992;98:41-104.

How to cite this article: Schussnig R, Rolf-Pissarczyk M, Bäumler K, Fries T-P, Holzapfel GA, Kronbichler M. On the role of tissue mechanics in fluid–structure interaction simulations of patient-specific aortic dissection. *Int J Numer Methods Eng*. 2024;e7478. doi: 10.1002/nme.7478

APPENDIX A. CONSTITUTIVE MODEL FRAMEWORK

The macroscopic anisotropic mechanical behavior of the aortic wall along with the underlying microstructure in the individual tissue layers are best captured using an anisotropic constitutive model. We specifically implemented the model proposed by Holzapfel et al.,[25] herein termed gHGO, which effectively represents the collagen fibers that are nonsymmetrically dispersed around their mean fiber orientation and embedded in the ground substance.

To achieve this, we first introduce the strain-energy function Ψ as

$$\Psi = \Psi(\mathbf{C}, \mathbf{H}), \tag{A1}$$

a function of the right Cauchy-Green tensor $\mathbf{C} = \mathbf{F}^{\mathrm{T}}\mathbf{F}$, which in turn is defined by the deformation gradient $\mathbf{F}$, as introduced in Section 3.1, and the generalized structure tensor $\mathbf{H}$. The generalized structure tensor characterizes the dispersion of collagen fibers oriented around their mean direction, which can be defined as

$$\mathbf{H} = \frac{1}{4\pi}\int_{\Phi=0}^{2\pi}\int_{\Theta=-\pi/2}^{\pi/2} \rho(\Phi,\Theta)\mathbf{N}(\Phi,\Theta)\otimes\mathbf{N}(\Phi,\Theta)\cos\Theta\,\mathrm{d}\Phi\mathrm{d}\Theta, \tag{A2}$$

with the property $\mathrm{tr}\,\mathbf{H} = 1$, and with

$$\mathbf{N}(\Phi,\Theta) = \cos\Theta\cos\Phi\mathbf{E}_1 + \cos\Theta\sin\Phi\mathbf{E}_2 + \sin\Theta\mathbf{E}_3, \tag{A3}$$

where $\mathbf{E}_1$, $\mathbf{E}_2$, and $\mathbf{E}_3$ are orthonormal basis vectors defining a Cartesian coordinate system in the reference configuration in which the vector $\mathbf{N}(\Phi,\Theta)$ describes the orientation of a single fiber within its fiber family. This orientation is characterized by two angles $\Phi \in [0, 2\pi]$ and $\Theta \in [-\pi/2, \pi/2]$. Consequently, all orientation vectors $\mathbf{N}(\Phi,\Theta)$ lie on the surface of a unit sphere. Note that the orthonormal basis vectors do not necessarily coincide with the mean fiber orientation and therefore need to be rotated to align with it. The generalized structure tensor is determined using a probability density function $\rho(\Phi,\Theta)$, which is integrated over the possible orientations on the surface of the unit sphere. We also need to satisfy the normalization condition given by

$$\frac{1}{4\pi}\int_{\Phi=0}^{2\pi}\int_{\Theta=-\pi/2}^{\pi/2} \rho(\Phi,\Theta)\cos\Theta\,\mathrm{d}\Phi\mathrm{d}\Theta = 1. \tag{A4}$$

Imaging results on collagen fiber dispersion in human aortic layers have indicated that the dispersion within the tangential plane is more significant than that in the out-of-plane direction.[101] Interestingly, the study[101] also revealed that the dispersions of the two planes are essentially independent. This independence suggests that the probability density function, particularly the bivariate von Mises distribution, as proposed by Holzapfel et al.,[25] can be multiplicatively decomposed as

$$\rho(\Phi,\Theta) = \rho_{\mathrm{in}}(\Phi)\rho_{\mathrm{op}}(\Theta), \tag{A5}$$

where $\rho_{\mathrm{in}}(\Phi)$ and $\rho_{\mathrm{op}}(\Theta)$ represent the in-plane and out-of-plane dispersion, respectively, with the properties $\rho_{\mathrm{in}}(\Phi) = \rho_{\mathrm{in}}(\Phi+\pi)$ and $\rho_{\mathrm{op}}(\Theta) = \rho_{\mathrm{op}}(-\Theta)$. The normalization condition introduced in Equation (A4) is now given by

$$\frac{1}{4\pi}\int_{\Phi=0}^{2\pi}\rho_{\mathrm{ip}}(\Phi)\,\mathrm{d}\Phi\int_{\Theta=-\pi/2}^{\pi/2}\rho_{\mathrm{op}}(\Theta)\cos\Theta\,\mathrm{d}\Theta = 1, \tag{A6}$$

determining the proportionality constant with in-plane and out-of-plane contributions, given by

$$\rho_{\text{in}}(\Phi) = \frac{\exp[b\cos(2\Phi)]}{I_0(a)} \quad \text{and} \quad \rho_{\text{op}}(\Theta) = 2\sqrt{\frac{2b}{\pi}}\frac{\exp[b\cos(2\Theta)]}{\exp(b)\text{erf}(\sqrt{2b})}, \tag{A7}$$

where $I_0(x)$ denotes the modified Bessel function of the first kind of order 0, $\text{erf}(x)$ is the error function, and a and b represent the concentration parameters of the distribution functions.

In our case only the diagonal components H_{11}, H_{22}, H_{33} of the generalized structure tensor $\mathbf{H}$ in the reference configuration are nonzero, so that $\mathbf{H}$ can be represented in the form

$$\mathbf{H} = H_{11}\mathbf{E}_1 \otimes \mathbf{E}_1 + H_{22}\mathbf{E}_2 \otimes \mathbf{E}_2 + H_{33}\mathbf{E}_3 \otimes \mathbf{E}_3. \tag{A8}$$

By using Equations (A2) and (A3) in addition to the probability density functions described in Equations (A5) and (A7), the diagonal components are explicitly specified by[102]

$$\begin{aligned} H_{11} &= \frac{1}{2}\left[1 + \frac{I_1(a)}{I_0(a)}\right]\left[1 - \frac{1}{4b} + \frac{\exp(-2b)}{\sqrt{2\pi b}\,\text{erf}(\sqrt{2b})}\right], \\ H_{22} &= \frac{1}{2}\left[1 - \frac{I_1(a)}{I_0(a)}\right]\left[1 - \frac{1}{4b} + \frac{\exp(-2b)}{\sqrt{2\pi b}\,\text{erf}(\sqrt{2b})}\right], \\ H_{33} &= \frac{1}{4b} - \frac{\exp(-2b)}{\sqrt{2\pi b}\,\text{erf}(\sqrt{2b})}, \end{aligned} \tag{A9}$$

in which $I_1(x)$ denotes the modified Bessel function of the first kind of order 1.

The strain-energy function Ψ can now be formulated for each layer, which describes the fiber alignment and dispersion for *two* fiber families i embedded in a ground substance. We assume here that the tissue is (nearly) incompressible, so that the determinant of the deformation gradient $J = \det \mathbf{F}$ approaches one. For the isotropic ground substance we follow a multiplicative decomposition of $\mathbf{F}$ into a dilatational part $J^{1/3}\mathbf{I}$ and a distortional part $\overline{\mathbf{F}} = J^{-1/3}\mathbf{F}$, see, for example, Gültekin et al.,[103] where $\mathbf{I}$ denotes the second-order unit tensor. We now assume that Ψ consists of a volumetric part Ψ_{vol}, a part Ψ_{g} that captures the ground substance, and a part Ψ_{c} that describes the contribution of two families of nonsymmetrically dispersed collagen fibers. Thus,

$$\Psi = \Psi_{\text{vol}}(J) + \Psi_{\text{g}}(\bar{I}_1) + \sum_{i=4,6}\Psi_{\text{c}}(\mathbf{C}, \mathbf{H}_i), \tag{A10}$$

where the first strain invariant of the symmetric modified Cauchy-Green tensor $\overline{\mathbf{C}} = \overline{\mathbf{F}}^{\text{T}}\overline{\mathbf{F}}$ is given by $\bar{I}_1 = \text{tr}\overline{\mathbf{C}}$, and $\mathbf{H}_i$ denote two generalized structure tensors related to the two fiber families embedded in a ground substance.

We can now derive the second Piola-Kirchhoff stress tensor $\mathbf{S}$ as[26]

$$\mathbf{S} = 2\frac{\partial\Psi}{\partial\mathbf{C}} = J\frac{\partial\Psi_{\text{vol}}(J)}{\partial J}\mathbf{C}^{-1} + 2J^{-2/3}\mathbb{P} : \frac{\partial\Psi_{\text{g}}(\bar{I}_1)}{\partial\bar{I}_1}\mathbf{I} + 2\sum_{i=4,6}\frac{\partial\Psi_{\text{c}}(\mathbf{C}, \mathbf{H}_i)}{\partial\mathbf{C}}, \tag{A11}$$

where $\mathbb{P} = \mathbb{I} - (1/3)\mathbf{C}^{-1} \otimes \mathbf{C}$ is a projection tensor in the Lagrangian setting and $(\mathbb{I})_{ABCD} = 1/2(\delta_{AC}\delta_{BD} + \delta_{AD}\delta_{BC})$ represents a fourth-order identity tensor.

The explicit expression for the volumetric energy Ψ_{vol} is assumed to be according to Simo and Miehe,[104] setting $\beta = -2$, and the ground substance is approximated by an isotropic neo-Hookean model, that is,

$$\Psi_{\text{vol}}(J) = \frac{\kappa_b}{4}\left(J^2 - 1 - 2\ln J\right), \qquad \Psi_{\text{g}}(\bar{I}_1) = \frac{\mu_s}{2}\left(\bar{I}_1 - 3\right), \tag{A12}$$

where κ_b is the bulk modulus according to (2) and $\mu_s > 0$ is the shear modulus of the ground substance in the reference configuration. The stress-strain response of the collagen fibers, which are responsible for the high nonlinear stiffening of

the aorta, is described by an exponential function that corresponds to the energy documented in Holzapfel et al.,[25] that is,

$$\Psi_c(\mathbf{C}, \mathbf{H}_i) = \frac{k_1}{2k_2}[\exp(k_2 E_i^2) - 1], \quad i = 4, 6, \tag{A13}$$

where $k_1 > 0$ is a stiffness-like parameter and $k_2 > 0$ is a dimensionless shape parameter, while

$$E_i = \mathbf{H}_i : (\mathbf{C} - \mathbf{I}) \tag{A14}$$

is a Green–Lagrange strain-like quantity that can be interpreted as an averaged or weighted fiber strain, depending on the fiber dispersion by the structure tensor $\mathbf{H}_i$, that is, Equation (A8) and the macroscopic deformation by $\mathbf{C}$. Since $\mathrm{tr}\mathbf{H}_i = 1$, we can write $E_i = \mathbf{H}_i : \mathbf{C} - 1$, using Equation (A14). We use the invariants I_i as switches, and assume that Ψ_c only contributes to the total energy Ψ when $I_4 > 1$ or $I_6 > 1$. Note that I_i are the squares of the stretches in the mean fiber directions.

Finally, we can rewrite Equation (A11) as

$$\boldsymbol{S} = \frac{\kappa_b}{2}\left(J^2 - 1\right)\boldsymbol{C}^{-1} + \mu_s J^{-2/3}\left(\boldsymbol{I} - \frac{1}{3} I_1 \boldsymbol{C}^{-1}\right) + 2\sum_{i=4,6} E_i k_1 [\exp(k_2 E_i^2)]\mathbf{H}_i. \tag{A15}$$

where the first strain invariant I_1 of the Cauchy-Green tensor $\mathbf{C}$ should not be confused with the modified Bessel function of the first kind of order 1 introduced in (A9). This relationship can then be inserted into Equation (1).

APPENDIX B. TRUE-TO-FALSE LUMEN PRESSURE DIFFERENCES

Tables B1–B4 supplement the results regarding the true-to-false lumen pressure differences as reported in Section 6.3 in the cross section at the LV level. The tables below contain the differences of the maximum (lower left half) and minimum (upper right half) between the true-to-false lumen pressure differences over the entire seventh cardiac cycle, calculated with the different models for the remaining cross sections at the LSA, PA, CT, and ABD levels. Differences are computed based on the true-to-false lumen pressure difference of the model in the row minus the value calculated by the model in the column and reported in mmHg. Comparison of results for any model other than the RWA and E800⋆ models therefore requires flipping the sign of the data relative to the target reference row to get a comparison set (see Section 6.3 for an example).

TABLE B1 Discrepancy between predictions of the true-to-false lumen pressure differences in the cross section at the LSA level in mmHg as obtained from the different models: differences in maximum (lower left half) and minimum (upper right half) $\Delta p_{TL/FL}$ over the entire seventh pulse cycle.

	RWA	E90	NH	gHGO	gHGO90	gHGO120	E20⋆	E50⋆	E100⋆	E800⋆
RWA	+0.00	−0.25	−0.72	−0.67	−0.28	−0.36	−0.33	−0.29	−0.04	+0.70
E90	+1.71	+0.00	−0.47	−0.42	−0.04	−0.11	−0.08	−0.05	+0.21	+0.95
NH	+1.95	+0.24	+0.00	+0.05	+0.43	+0.36	+0.39	+0.42	+0.67	+1.42
gHGO	+2.50	+0.80	+0.55	+0.00	+0.38	+0.31	+0.34	+0.37	+0.62	+1.37
gHGO90	+2.12	+0.41	+0.17	−0.39	+0.00	−0.08	−0.05	−0.01	+0.24	+0.99
gHGO120	+2.22	+0.52	+0.27	−0.28	+0.11	+0.00	+0.03	+0.07	+0.32	+1.06
E20⋆	+1.24	−0.47	−0.71	−1.27	−0.88	−0.99	+0.00	+0.04	+0.29	+1.03
E50⋆	+1.26	−0.45	−0.69	−1.25	−0.86	−0.97	+0.02	+0.00	+0.25	+0.99
E100⋆	+3.32	+1.62	+1.37	+0.82	+1.21	+1.10	+2.09	+2.06	+0.00	+0.74
E800⋆	+5.72	+4.01	+3.77	+3.21	+3.60	+3.49	+4.48	+4.46	+2.40	+0.00

Note: The difference between row *i* and column *j* is calculated as the value from the model in row *i* minus the value from the model in column *j*.

TABLE B2 Discrepancy between predictions of the true-to-false lumen pressure differences in the cross section at the PA level in mmHg as obtained from the different models: differences in maximum (lower left half) and minimum (upper right half) $\Delta p_{TL/FL}$ over the entire seventh pulse cycle.

	RWA	E90	NH	gHGO	gHGO90	gHGO120	E20⋆	E50⋆	E100⋆	E800⋆
RWA	+0.00	−0.89	−1.39	−1.46	−1.34	−1.71	−1.38	−1.07	−0.67	−0.51
E90	+2.40	+0.00	−0.50	−0.57	−0.45	−0.82	−0.49	−0.18	+0.22	+0.38
NH	+2.21	−0.19	+0.00	−0.07	+0.06	−0.31	+0.01	+0.32	+0.72	+0.89
gHGO	+2.56	+0.16	+0.35	+0.00	+0.12	−0.25	+0.07	+0.39	+0.78	+0.95
gHGO90	+2.45	+0.05	+0.24	−0.11	+0.00	−0.37	−0.05	+0.27	+0.66	+0.83
gHGO120	+2.23	−0.17	+0.02	−0.33	−0.23	+0.00	+0.32	+0.64	+1.03	+1.20
E20⋆	+2.08	−0.32	−0.13	−0.48	−0.38	−0.15	+0.00	+0.32	+0.71	+0.88
E50⋆	+1.80	−0.60	−0.41	−0.76	−0.65	−0.42	−0.27	+0.00	+0.39	+0.56
E100⋆	+3.07	+0.67	+0.86	+0.51	+0.62	+0.85	+1.00	+1.27	+0.00	+0.17
E800⋆	+4.16	+1.76	+1.95	+1.60	+1.71	+1.93	+2.08	+2.36	+1.09	+0.00

Note: The difference between row *i* and column *j* is calculated as the value from the model in row *i* minus the value from the model in column *j*.

TABLE B3 Discrepancy between predictions of the true-to-false lumen pressure differences in the cross section at the CT level in mmHg as obtained from the different models: differences in maximum (lower left half) and minimum (upper right half) $\Delta p_{TL/FL}$ over the entire seventh pulse cycle.

	RWA	E90	NH	gHGO	gHGO90	gHGO120	E20⋆	E50⋆	E100⋆	E800⋆
RWA	+0.00	−5.09	−5.72	−5.51	−5.37	−5.81	−5.52	−3.23	−5.07	−2.79
E90	+0.07	+0.00	−0.63	−0.42	−0.27	−0.72	−0.42	+1.87	+0.02	+2.30
NH	−0.28	−0.35	+0.00	+0.21	+0.36	−0.09	+0.21	+2.50	+0.65	+2.93
gHGO	−0.03	−0.10	+0.25	+0.00	+0.14	−0.30	−0.00	+2.28	+0.44	+2.72
gHGO90	−0.01	−0.08	+0.27	+0.02	+0.00	−0.45	−0.15	+2.14	+0.30	+2.58
gHGO120	−0.17	−0.24	+0.11	−0.14	−0.16	+0.00	+0.30	+2.59	+0.74	+3.02
E20⋆	−1.17	−1.23	−0.88	−1.14	−1.15	−1.00	+0.00	+2.29	+0.45	+2.72
E50⋆	+2.06	+1.99	+2.34	+2.09	+2.07	+2.23	+3.22	+0.00	−1.84	+0.44
E100⋆	+1.79	+1.72	+2.07	+1.82	+1.80	+1.96	+2.95	−0.27	+0.00	+2.28
E800⋆	+0.66	+0.59	+0.94	+0.69	+0.67	+0.83	+1.83	−1.40	−1.13	+0.00

Note: The difference between row *i* and column *j* is calculated as the value from the model in row *i* minus the value from the model in column *j*.

TABLE B4 Discrepancy between predictions of the true-to-false lumen pressure differences in the ABD cross section in mmHg as obtained from the different models: differences in maximum (lower left half) and minimum (upper right half) $\Delta p_{TL/FL}$ over the entire seventh pulse cycle.

	RWA	E90	NH	gHGO	gHGO90	gHGO120	E20⋆	E50⋆	E100⋆	E800⋆
RWA	+0.00	−3.30	−3.82	−3.86	−3.77	−3.97	−1.89	−0.46	−1.95	−1.31
E90	+1.52	+0.00	−0.52	−0.56	−0.47	−0.67	+1.41	+2.84	+1.35	+1.99
NH	+1.55	+0.03	+0.00	−0.04	+0.04	−0.15	+1.93	+3.36	+1.86	+2.51
gHGO	+1.60	+0.08	+0.05	+0.00	+0.09	−0.11	+1.97	+3.40	+1.90	+2.55
gHGO90	+1.38	−0.14	−0.17	−0.22	+0.00	−0.20	+1.89	+3.31	+1.82	+2.46
gHGO120	+1.00	−0.52	−0.55	−0.60	−0.38	+0.00	+2.08	+3.51	+2.02	+2.66
E20⋆	+2.34	+0.82	+0.79	+0.74	+0.96	+1.34	+0.00	+1.43	−0.07	+0.58
E50⋆	+3.39	+1.87	+1.83	+1.79	+2.01	+2.38	+1.05	+0.00	−1.50	−0.85
E100⋆	+2.65	+1.13	+1.10	+1.05	+1.27	+1.65	+0.31	−0.73	+0.00	+0.64
E800⋆	+3.11	+1.59	+1.56	+1.51	+1.73	+2.11	+0.77	−0.27	+0.46	+0.00

Note: The difference between row *i* and column *j* is calculated as the value from the model in row *i* minus the value from the model in column *j*.